

Epitaxial RuO₂ and IrO₂ films by pulsed laser deposition on TiO₂(110)

P. Keßler,^{1,2} T. Waldsauer,^{1,2} V. Jovic,^{3,4} M. Kamp,^{1,5} M. Schmitt,^{1,2} M. Sing,^{1,2} R. Claessen,^{1,2} and S. Moser^{1,2}

^{1)Physikalisches Institut, Universität Würzburg, 97074 Würzburg, Germany}

^{2)Würzburg-Dresden Cluster of Excellence ct.qmat, Universität Würzburg, 97074 Würzburg, Germany}

^{3)Earth Resources and Materials, Institute of Geological and Nuclear Science, 5010 Lower Hutt, New Zealand}

^{4)MacDiarmid Institute for Advanced Materials and Nanotechnology, 6012 Wellington, New Zealand}

^{5)Röntgen Center for Complex Material Systems, Universität Würzburg, 97074 Würzburg, Germany}

(*Electronic mail: simon.moser@uni-wuerzburg.de)

(Dated: 22 May 2024)

We present a systematic growth study of epitaxial RuO₂(110) and IrO₂(110) on TiO₂(110) substrates by pulsed laser deposition. We describe the main challenges encountered in the growth process, such as a deteriorating material flux due to laser induced target metallization or the delicate balance of under- vs over-oxidation of the 'stubborn' Ru and Ir metals. We identify growth temperatures and oxygen partial pressures of 700 K, 1×10^{-3} mbar for RuO₂ and 770 K, 5×10^{-4} mbar for IrO₂ to optimally balance between metal oxidation and particle mobility during nucleation. In contrast to IrO₂, RuO₂ exhibits layer-by-layer growth up to 5 unit cells if grown at high deposition rates. At low deposition rates, the large lattice mismatch between film and substrate fosters initial 3D island growth and cluster formation. In analogy to reports for RuO₂ based on physical vapor deposition,¹ we find these islands to eventually merge and growth to continue in a step flow mode, resulting in highly crystalline, flat, stoichiometric films of RuO₂(110) (up to 30 nm thickness) and IrO₂(110) (up to 13 nm thickness) with well defined line defects.

I. INTRODUCTION

The binary oxides of ruthenium (RuO₂) and iridium (IrO₂) are functional Dirac semi-metals that have recently attracted considerable interest in both applied and fundamental materials science.²⁻⁵ They both are important co-catalysts for the oxygen evolution reaction (OER) in electrocatalytic water splitting, with RuO₂ being more active, but IrO₂ being more corrosion resistant.^{2,6-9} Their catalytic efficiency depends on crystal size and surface orientation,^{10,11} on surface order and stoichiometry,^{12,13} as well as on the lattice structure of the supporting substrate.¹⁴

RuO₂ is the only stable solid oxide phase of ruthenium and crystallizes in a non-symmorphic rutile crystal structure ($a = b = 4.48 \text{ \AA}$, $c = 3.11 \text{ \AA}$, space group 136: P4₂/mnm).¹⁵ With its Fermi level well positioned within the t_{2g} derived conduction band, it is a good electrical conductor that below 2 K can be tuned into the superconducting regime by epitaxial strain.^{16,17} The metallic conductivity of RuO₂ as well as its favorable thermal and chemical stability are the main reasons for its industrial utility, e.g., as contact material in microelectronic devices¹⁸ or as electrocatalyst in a variety of oxidation and dehydrogenation reactions.^{2,7} The Fermi surface of RuO₂ was characterized by transport and calorimetric methods in the 1970s,¹⁹ and recently mapped by angle resolved photoemission spectroscopy (ARPES).^{20,21} The non-symmorphic crystal structure of the RuO₂ rutile lattice produces a Fermi surface composed of Dirac nodal lines (DNL).²⁰⁻²² Strong nesting of these DNLs might be prone to Fermi surface instabilities,²³ a postulated driving force of collinear magnetic ordering in RuO₂ that was derived from

neutron²⁴ and resonant x-ray scattering,^{25,26} but recently challenged by muon spin rotation experiments.^{27,28}

In unison with the crystal field, this collinear order would produce a non-relativistic spin splitting that breaks time reversal symmetry in the band structure of RuO₂, and is thus consistent with recent observations of the anomalous Hall effect (AHE),^{33,34} spin transfer torque,³⁵ and giant tunneling magnetoresistance³⁶ in RuO₂ thin film structures. RuO₂ would thus classify as a so called *altermagnet*, i.e., as a compensated collinear magnet of net zero magnetization, whose spin splitting alternates in reciprocal space, setting altermagnets fundamentally apart from ferro- and antiferromagnets.^{37,38} RuO₂ thus lends itself as a formidable playground to study the intimate relationship between its structural, electronic and magnetic properties that potentially culminate in altermagnetism.

IrO₂ on the other hand ($a = b = 4.51 \text{ \AA}$, $c = 3.18 \text{ \AA}$, space group 136: P4₂/mnm),¹⁵ the 5d sister compound of RuO₂, offers itself as useful comparative material to benchmark potential altermagnetism in RuO₂. It shares the non-symmorphic rutile crystal structure and thus the spin orbit gapped DNL structure with RuO₂,^{22,39} and was shown to also exhibit exotic experimental effects such as spin-orbit torque,^{40,41} electrochromism,^{42,43} an inverse spin-Hall effect⁴⁴ and magnetic field dependent charge carrier switching.⁴⁵ In contrast to RuO₂, however, consensus about Pauli paramagnetism in IrO₂ remains unchallenged, even though a slight ferromagnetic order seems to be theoretically possible.⁴⁶

A meaningful investigation of such physical phenomena requires reproducible samples of excellent crystallinity and well defined stoichiometry.⁴⁷ In this work, we thus optimized the epitaxial synthesis of RuO₂ and IrO₂ thin films on TiO₂(110)

Material	Substrate	Growth parameters
Method	Lattice	Evaluation of growth process
Reference	Mismatch ¹⁵	
RuO₂(110)	Ru(0001)	$T = 650\text{ K}$, O ₂ -exposure: $2 \times 10^6\text{ L}$
Substrate oxidation	[001]: 13.0 %	Scanning tunneling microscopy indicates a well ordered RuO ₂ (110) surface with small regions of RuO ₂ (100) growth. Annealing above 500 K partly restores a damaged surface.
Over (2004) ²⁹	[110]: -11.0 %	
RuO₂(100)	Ru(1010)	$T = 700\text{ K}$, O ₂ -exposure: $3 \times 10^5\text{ L}$
Substrate oxidation	[001]: 13.0 %	After oxidation, a predominating RuO ₂ (100) surface is accompanied by regions of RuO ₂ (110), RuO ₂ (101) as well as an catalytically inactive RuO ₂ (100)-c(2x2) phase.
Over (2004) ²⁹	[010]: 4.8 %	
RuO₂(110)	TiO ₂ (110)	$T = 600\text{ K}$, $p(\text{O}_2) = 1 \times 10^{-6}\text{ mbar}$
PVD	[001]: 4.9 %	A well ordered film with surface clusters resulting from island merging. The XPS area ratio of the screened and unscreened Ru 3d peaks hints to a non-stoichiometric film composition.
He (2015) ¹	[110]: -2.6 %	
RuO₂(110)	MgO(001)	$T = 970\text{ K}$, $p(\text{O}_2) = 9 \times 10^{-4}\text{ mbar} - 1 \times 10^{-1}\text{ mbar}$, $F = 0.45\text{ J/cm}^2$, $\lambda = 193\text{ nm}$
PLD	[001]: -1.1 %	The best crystalline quality is achieved for films grown at 970 K. Changing the oxygen pressure influenced the growth rate, but lead to no / small changes of the crystalline quality.
Fang (1997) ³⁰	[110]: 0.8 %	
RuO₂(200)	LaAlO ₃ (001)	$T = 770\text{ K}$, $p(\text{O}_2) = 1 \times 10^{-1}\text{ mbar}$, $F = 3\text{ J/cm}^2$, $\lambda = 248\text{ nm}$
PLD	[011]: 2.0 %	AFM suggests a transition from layer-by-layer to island growth at a film thickness of 7 RuO ₂ unit cells.
Wang (2006) ³¹	n.a.	
RuO₂(001)	TiO ₂ (001)	$T = 970\text{ K}$, $p(\text{O}_2) = 6.7 \times 10^{-3}\text{ mbar} - 6.7 \times 10^{-2}\text{ mbar}$, $F = 2\text{ J/cm}^2$, $\lambda = 248\text{ nm}$
PLD	[010]: -2.6 %	The RuO ₂ sheet resistance can be reduced by applying a lower $p(\text{O}_2)$ during growth ($6.7 \times 10^{-2} - 1.3 \times 10^{-2}\text{ mbar}$). AFM reveals island growth for a 10 nm thick RuO ₂ film.
Kim (2019) ³²	[100]: -2.6 %	

TABLE I. Literature review of single crystalline RuO₂ thin film synthesis. Summarized are the respective fabrication method, the substrate type and orientation, the growth parameters along with a short summary of the study. The lattice mismatch is calculated based on structural data summarized in Ref.¹⁵ according to the formula $1 - a_{\text{substrate}}/a_{\text{film}}$, where a is the respective lattice constant. The following symbols are used to describe physical quantities: T : substrate temperature; $p(\text{O}_2)$: oxygen partial pressure; F : deposition laser fluency; λ : deposition laser wavelength; L : dosage (1L = 1 Langmuir = 1.33×10^{-6} mbars).

substrates by pulsed laser deposition (PLD), and report the individual growth modes, defect structures and trends that we encountered in our extensive in- and ex-situ chemical and structural analysis. Specifically, we demonstrate the PLD film growth of stoichiometric, uniform, closed and thickness controlled epitaxial RuO₂(110) (up to 30 nm) and IrO₂(110) (up to 13 nm) films on TiO₂(110) substrates of high crystalline quality with few well defined line defects and suppressed island formation.

To achieve this goal, we performed a systematic exploration of the multidimensional growth control parameter space, including target and laser flux as well as substrate temperature and oxygen partial pressure. We thoroughly analyzed this growth matrix by a combination of *in situ* and *ex situ* microspectroscopy techniques, identifying the individual growth modes along with the optimal parameter set for epitaxial film growth and the most common defect structures. In the following, we detail out the technical challenges for the PLD growth of RuO₂ and IrO₂, and highlight the most pertinent commonalities and differences encountered in these two material systems.

II. STATE-OF-THE-ART RuO₂ AND IrO₂ EPITAXIAL SYNTHESIS

Fabrication methods of crystalline RuO₂ and IrO₂ are extensive and outlined in excellent reviews.^{2,4,5} Here, we are exclusively interested in the synthesis of RuO₂ and IrO₂ thin films of high bulk and surface crystalline order and provide a detailed summary of literature reports in Tab. I and Tab. II for both materials. In addition to this overview, much progress in sample production was carried by (i) the oxidation of Ru(0001), Ru(1010), Ir(111) and Ir(100) single crystal surfaces (RuO₂: Refs. 29, 53–55, IrO₂: Refs. 48, 49, 56, and 57) as well as a variety of different bottom-up growth procedures such as (ii) molecular beam epitaxy (MBE, RuO₂: Refs. 58 and 59, IrO₂: Refs. 45, 50, 60–63), (iii) pulsed laser deposition (PLD, RuO₂: Refs. 30–32, and 64, IrO₂: Refs. 11, 52, 65–70), (iv) physical vapor deposition (PVD, RuO₂, Ref. 1, IrO₂: Ref. 53), (v) reactive magnetron sputtering (RuO₂: Refs. 71–75, IrO₂: Refs. 76–82), (vi) atomic layer deposition (ALD, RuO₂: Refs. 31, 83–86, IrO₂: Refs. 87–91), or more recently (vii) thermal laser epitaxy (TLE, RuO₂: Ref. 92). To our knowledge, high quality single crystalline thin films with a well defined surface orientation to date have solely been reported from methods (i) single crystal oxida-

Material	Substrate	Growth parameters
Method	Lattice	Evaluation of growth process
Reference	Mismatch ¹⁵	
IrO₂(110) / (100)	Ir(111)	$T = 775 \text{ K} - 875 \text{ K}$, $p(\text{O}_2) = 100 \text{ mbar}$
Substrate oxidation	[001]: 14.2 %	The bulklike IrO ₂ mainly consists of domains with an (110) and (100) oriented surface. Changing the oxidation parameters leads to the formation of an O-Ir-O trilayer as well as to corundum (Ir ₂ O ₃).
He (2008) ⁴⁸	[110]: 25.9 %	
IrO₂(100)	Ir(111)	$T = 600 \text{ K}$, O-plasma: $3.6 \times 10^5 \text{ L}$
Substrate oxidation	[001]: 14.2 %	Applying an oxygen plasma enables the selective preparation of a pure IrO ₂ (100) phase without IrO ₂ (110) domains. Corundum can also be obtained for higher plasma exposures.
Chung (2012) ⁴⁹	[010]: -4.8 %	
IrO₂(110)	TiO ₂ (110)	$T = 570 \text{ K}$, $p(\text{O}_2) = 6.67 \times 10^{-6} \text{ mbar}$
MBE	[001]: 6.8 %	Production of high phase purity films by solid-source metal-organic MBE from 3 - 50 monolayer thickness. The ratio between Ir and IrO ₂ can be engineered by epitaxial strain.
Nair (2023) ⁵⁰	[110]: -2.1 %	
IrO₂(110)	MgO(001)	$T = 1020 \text{ K}$, $p(\text{O}_2) = 2.67 \times 10^{-1} \text{ mbar}$, $\lambda = 248 \text{ nm}$
PLD	[001]: 1.0 %	A BaTiO ₃ buffer layer is needed to prevent the formation of IrMg intermetallics. XRD indicates a single domain film and AFM shows island growth with a root-mean-square roughness of $\approx 6 \text{ nm}$.
Stoerzinger (2014) ¹¹	[110]: 1.3 %	
IrO₂(100)	SrTiO ₃ (100)	$T = 670 \text{ K} - 870 \text{ K}$, $p(\text{O}_2) = 5 \times 10^{-2} \text{ mbar} - 1 \text{ mbar}$, $F = 0.5 \text{ J/cm}^2 - 0.7 \text{ J/cm}^2$, $\lambda = 248 \text{ nm}$
PLD	[202]: -0.4 %	The thin films are insulating due to island growth up to a film thickness of 25 nm. Thicker films of 40 nm show metallic transport behaviour likely resulting from a continuous but granular structure.
Bhat (2017) ⁵¹	n.a.	
IrO₂(110)	TiO ₂ (110)	$T = 770 \text{ K}$, $\lambda = 248 \text{ nm}$
PLD	[001]: 6.8 %	The IrO ₂ (110) films were grown up to a thickness of 92.2 nm. Data on the morphology of the sample was not provided in this study.
Arias (2021) ⁵²	[110]: -2.1 %	
IrO₂(110)	RuO ₂ (110)	$T = 700 \text{ K}$, $p(\text{O}_2) = 3 \times 10^{-7} \text{ mbar}$, $\lambda = 248 \text{ nm}$
PVD	[001]: 2.1 %	The IrO ₂ films with a thickness of up to 10 nm exhibit a high crystalline and surface quality. They are prepared by an initial nucleation step that is followed by layer-by-layer growth.
Abb (2018) ⁵³	[110]: 0.5 %	

TABLE II. Literature review of single crystalline IrO₂ thin film synthesis. Summarized are the respective fabrication method, the substrate type and orientation, the growth parameters along with a short summary of the study. The lattice mismatch is calculated based on structural data summarized in Ref.¹⁵ according to the formula $1 - a_{\text{substrate}}/a_{\text{film}}$, where a is the respective lattice constant. The following symbols are used to describe physical quantities: T : substrate temperature; $p(\text{O}_2)$: oxygen partial pressure; F : deposition laser fluency; λ : deposition laser wavelength; L : dosage (1L = 1 Langmuir = 1.33×10^{-6} mbars).

tion (RuO₂: Ref. 29, IrO₂: Refs. 48 and 49), from (ii) MBE (IrO₂, Ref. 50), (iii) PLD (RuO₂: Refs. 30–32, IrO₂: Refs. 11, 51, and 52), and from (iv) PVD (RuO₂, Ref. 1, IrO₂: Ref. 53). The respective results are reviewed in Tabs. I and II.

In method (i), single Ru(0001), Ru(1010), Ir(111) or Ir(100) crystal surfaces are prepared by repeated cycles of sputtering and annealing to form a clean, well ordered surface, as well as subsequent thermal flashing in oxygen to remove residual carbon contamination. The oxide layer is then formed in a following oxidation step at elevated temperatures (Tabs. I and II), which results in oxide flakes with a well ordered crystal surface.^{29,48} While such samples can be well suited for some surface spectroscopy as well as catalytic experiments,⁹³ they are limited by the low achievable film thickness of only a few nanometers,^{48,94,95} by the formation of multi-domain structures with different surface orientations due to the substrate symmetry,^{54,94} as well as by the metallicity of the substrate that prevents meaningful transport experiments in the oxide over-layer.

Alternatively, RuO₂ and IrO₂ films have been grown on insulating single crystal substrates of varying lattice param-

eters and surface orientations. The most usual substrates along with their lattice mismatches to RuO₂ and IrO₂, the respective sample growth parameters, and a brief summary of the growth process and resulting crystalline quality are summarized in Tab. I and Tab. II. The most commonly used substrate material is rutile TiO₂. Beyond the commercial availability of high quality polished wafers of variable surface orientation at acceptable cost, its isostructural crystal lattice with regards to RuO₂ and IrO₂ enables epitaxial growth without the formation of rotational domains. This allows for experiments that depend explicitly on the crystal orientation, such as bulk transport^{33,34,40} or surface catalytic measurements.^{11,13} While the lattice constants of the materials are comparable, their mismatch to TiO₂ is still significant with 4.9% and -2.6% along [001] and [110] for RuO₂,⁵⁸ as well as 6.8% and -2.1% along [001] and [110] for IrO₂.¹⁵ This fosters the formation of defects and disorder in the epitaxial films resulting from strain release.

To cope with problems arising due to the lattice mismatch induced strain, different strategies have been reported in literature including the growth of material at a reduced deposi-

tion rate,^{30,96} the application of a temperature gradient across the substrate to induce an initial intermixing of substrate and film,⁵⁸ the growth of islands,^{31,32} and the coalescence of such initial islands (island merging) followed by a final step flow process.¹ Moreover, the lattice mismatch can also be used for strain engineering, e.g., to induce superconductivity in RuO₂,¹⁷ or to reduce the formation of metallic Ir droplets at the surface of IrO₂.⁵⁰

Comparing the methods that are commonly employed in the synthesis of low dimensional RuO₂ and IrO₂ samples, we notice a variety of problems that are specific to the individual deposition technique, and mostly relate to the low vapor pressure of Ru, Ir and their oxides in combination with high oxidation potentials. In MBE, e.g., the high source temperatures needed to evaporate the metal in combination with high oxygen partial pressures^{17,97} require the use of customized reactive-oxide MBEs to minimize the risk of corroding (oxidizing) machine components. To minimize this effect, atomic oxygen or ozone is typically used to locally increase the oxidation potential right at the substrate.¹⁷ Further, the metal vapor pressure can be artificially increased and the source temperature consequently decreased by applying metal organic precursors.⁵⁰

While these drawbacks of MBE are probably most optimally solved by the adsorption controlled TLE approach,^{92,98} they can also be appropriately addressed by the more common PLD method where a strong pulsed laser ablates the target material pulse by pulse. The plasma that forms in this way is ill defined and the deposited material does not arrive uniformly on the substrate surface.⁹⁹ This has to be counteracted by additional reactive oxygen, and thus pushes PLD far off the adsorption-controlled limit. In PLD of RuO₂ and IrO₂, in particular, we further find a considerable loss of target oxygen upon ablation, leading to a massive increase in target reflectivity and a consequent drop in deposition rate, which ultimately limits the achievable film thickness. In combination with the well-known coating problem of the deposition laser entry window, this is likely the reason why a wide range of laser energy densities has been reported in the PLD literature for RuO₂^{30–32,96} and IrO₂^{100,101} growth. This might also be the reason why to date – at least to our knowledge – there are no reports on the PLD growth of epitaxial RuO₂ and IrO₂ thin films with high quality bulk as well as surface order as achieved, e.g., by MBE.^{1,50}

III. EXPERIMENTAL DETAILS

The sample growth was conducted in a commercially available PLD setup (TSST B.V.) with a base pressure typically below 5×10^{-9} mbar. The substrate temperature was controlled by a laser heating setup ($\lambda = 976$ nm, ComPACT-Evolution DILAS), where the temperature is measured by a two-color pyrometer (IMPAC) directed to the backside of a 1 mm thick, sandblasted Inconel sample holder. A capillary, mounted at a distance of 10 cm from the substrate, directs N5.5 oxygen at its surface to locally adjust the oxygen partial pressure. The pressure is measured by a Pfeiffer full range gauge mounted

on the chamber walls, resulting in an effectively higher pressure at the sample. The targets are placed at a distance of 55 mm in front of the substrate and are ablated by an excimer laser ($\lambda = 248$ nm, COMPEX Pro 205/KrF). The growth was monitored by a reflection high-energy electron diffraction setup (RHEED, Staib Instruments: CB801420) that was operated at electron energies of 30 keV. The PLD chamber is connected *in vacuo* to an x-ray photoelectron spectroscopy (XPS, Scienta Omicron) setup with a monochromatic Al K α X-ray source of 1486.7 eV, and to a low-energy electron diffraction system (LEED, Omicron: SPECTALEED) with a LaB₆ cathode. *Ex-situ* measurements include atomic force microscopy (AFM, VEECO, tapping mode in air), scanning transmission electron microscopy (STEM, uncorrected FEI Titan 80-300, 300 kV, 100 - 200 pA), scanning electron microscopy (SEM, Zeiss Ultra Plus, 15 kV) including energy-dispersive X-ray spectroscopy (EDX), as well as X-ray diffraction (XRD) and reflectivity (XRR, BRUKER, Cu K α 8.05 keV).

A. TiO₂(110) substrate preparation

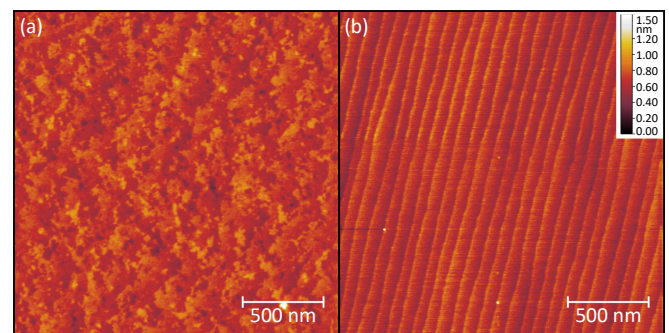


FIG. 1. Atomic force microscope measurements of TiO₂(110) substrate: (a) Untreated substrate as delivered. (b) Stepped terrace surface after two step ultrasonic cleaning and tube furnace annealing.

For the film growth, we employed (110) terminated TiO₂ substrates supplied by Crystal GmbH, Berlin, Germany. The untreated substrates show a surface with randomly sized patches of a few atoms height difference as shown in Fig. 1 (a). To remove surface contamination, the substrates were initially cleaned for 20 minutes in subsequent ultrasonic baths of acetone and isopropyl alcohol. Following a protocol developed for TiO₂(001),¹⁰² we further annealed these substrates in a tube furnace at 820 °C under an oxygen flow of 20 l/h for 5 h. This annealing step routinely yields well-defined TiO₂(110) surfaces with a stepped terrace morphology as shown in Fig. 1 (b). As XPS and EDX on our RuO₂ films occasionally revealed calcium contamination that likely resulted from polish residues of our commercial substrates, the TiO₂(110) employed for the IrO₂ growth was further treated by a short etching step ($t = 5$ min, ultrasonic bath) in 6:1 buffered hydrofluoric acid. After etching, the substrates were rinsed by high-purity water and the acetone / isopropyl cleaning step was repeated. Substrates that were treated in this way did no longer exhibit the calcium contamination.

B. Target control

For the RuO_2 film growth, we used a disk-shaped commercial target (TOSHIMA manufacturing Co. Ltd.) from compressed and sintered RuO_2 powder. Ablation was achieved by scanning the target relative to the fixed ablation laser spot at a constant scan rate of 1.5 mm/s. The scanning area was 37.5 mm^2 (gray stripes in Figs. 2 (a) and (b)), determined by the laser spot width of 2.5 mm, and the scanning width of 15.0 mm that is limited by the target diameter. Repeated scanning of the same target area increases the target reflectivity and leads to a steady reduction of the deposition rate. For a given film growth, we thus typically scanned two fresh, separate target regions, which resulted in a total ablated area of 75.0 mm^2 (Fig. 2 (b)).

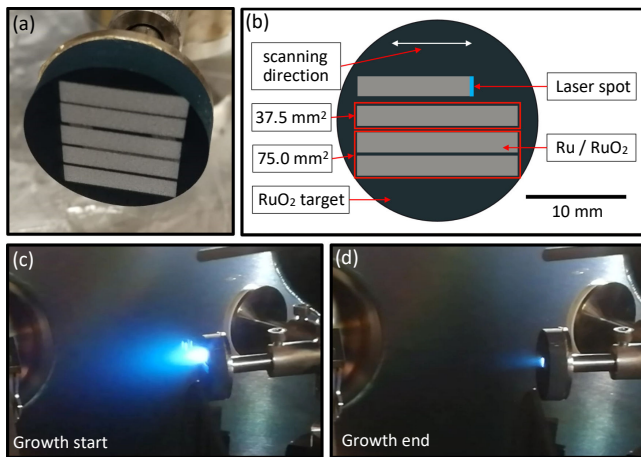


FIG. 2. (a) RuO_2 target metallization due to laser ablation. (b) Definition of the target areas. Size of the plasma plume at (c) the start and (d) the end of the film growth.

The IrO_2 target was manufactured in house using a 99.9 % pure trace metal basis IrO_2 powder supplied by Sigma-Aldrich. After X-ray powder diffraction to confirm the crystalline structure, the IrO_2 powder was ground to obtain a uniform grain size and then compressed for 5 minutes by a force of 50 kN. In a subsequent annealing step at 870°C , the target was sintered for 12 h under an oxygen flow of 25 l/h to increase its solidity. The ablated target area was limited to 12 mm^2 due to cracks in the target disk. However, we recommend a larger scanning area – similar to the one used for RuO_2 growth – due to a rapid loss of oxygen and consequent metallization of the target surface that drastically increases its reflectivity.

Every RuO_2 and IrO_2 film reported in this study was grown from a freshly prepared target surface. Once the entire target surface was consumed, it was revived by sanding off the reflective surface layer *ex vacuo*.

C. Material flux control

Based on these targets, we then optimized the material flux through control of the laser fluency on the target. As noted in the introduction and the paragraph above, a serious technical challenge in the PLD growth of RuO_2 and IrO_2 thin films lies in the decrease of material deposition rate despite a constant laser fluency. This is mostly due to the consecutive oxygen depletion of the target upon ablation, resulting in an increase in target metallicity/reflectivity (at 248 nm from 22% on IrO_2 to 70% on Ir, and from 20% on RuO_2 to 60% on Ru),^{103,104} and a concomitant decrease in energy absorption and material flux during the film growth (Fig. 2 (a)). This change in material flux can be observed visually as a considerable shrinkage of the plasma plume during ablation: Applying 2,000 laser pulses at standard growth parameters ($p(\text{O}_2) = 1 \times 10^{-3}$ mbar, $J = 0.7 \text{ J/cm}^2$) to a RuO_2 target, e.g., changes the plasma plume from being extended over a few cm in Fig. 2 (c) to being barely visible in Fig. 2 (d).

Aiming at saturating the target reflectivity and thus achieving a more uniform material flux, we pre-ablated the fresh target by 2,000 laser pulses at closed shutter before the actual growth was started. As we observed a significant increase in target reflectivity and subsequent decrease of the material flux even after this step, we turned to gradually increasing the laser energy density during growth to compensate for the target depletion. Reasonable material flux stability was achieved by a step-wise increase of the laser energy density from 0.7 J/cm^2 to 1.4 J/cm^2 , using steps of 0.1 J/cm^2 after every 2,000 laser pulses. For RuO_2 , this resulted in a total amount of 16,000 laser pulses until the 37.5 mm^2 scanning area was fully consumed. While this pre-ablation and subsequent ramp-up protocol during growth lends itself to future optimization, we note that, in general, the maximum film thickness achievable by PLD is mostly limited by the available target surface area and the maximum laser fluency. The overall control of material flux is, however, rather limited.

A second but well known reason for a decreased material flux is the deposition of ablated material onto the deposition laser entry window. The deposited material hereby acts as a low transmissivity coating that reduces the laser energy density at the target. To determine the reduction of material flux by this coating process, we initially cleaned the laser entry window and then successively grew two RuO_2 films at identical growth parameters of 700 K substrate temperature and 1×10^{-3} mbar oxygen partial pressure, both times applying a total amount of 64,000 laser pulses per film while scanning across four fresh 37.5 mm^2 target areas and increasing the laser energy density as described above. Although the growth parameters for both films were thus virtually identical, an analysis of XRR data yielded a film thickness of 30(1) nm for the first film, and 22(1) nm for the second film (Fig. 3 (a)). This 25 % reduction of film thickness indicates a severe loss in transparency of the laser entry window, implying a notorious difficulty to reproduce identical film thicknesses if the transparency of the laser entry window is not reset before each individual film growth. Interestingly, the reduction of laser fluency due to the window coating also induces a change in

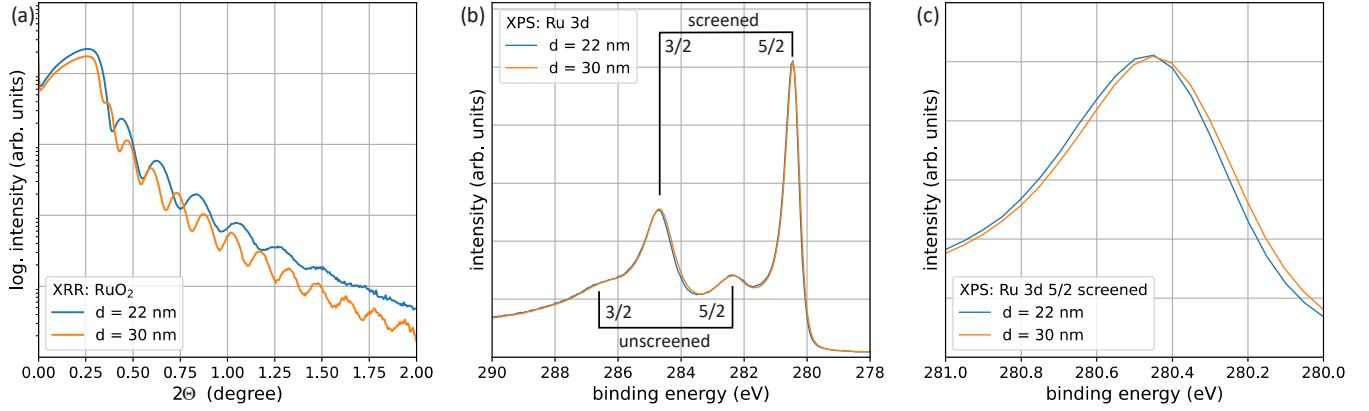


FIG. 3. (a) XRR measurements of two RuO_2 films that were grown consecutively at nominally identical growth parameters. While the first film is 30 nm thick, a reduction in the deposition rate due coating of the laser entry window yields only a thickness of 22 nm for the second film. (b) XPS measurements of both films, highlighting the unscreened (u) and screened (s) contributions to the Ru 3d 5/2 and 3/2 multiplets, respectively. A closeup in (c) of the screened Ru 3d 5/2 peak highlights the second film to be slightly less metallic than the first one, indicated by a shift to lower binding energies.

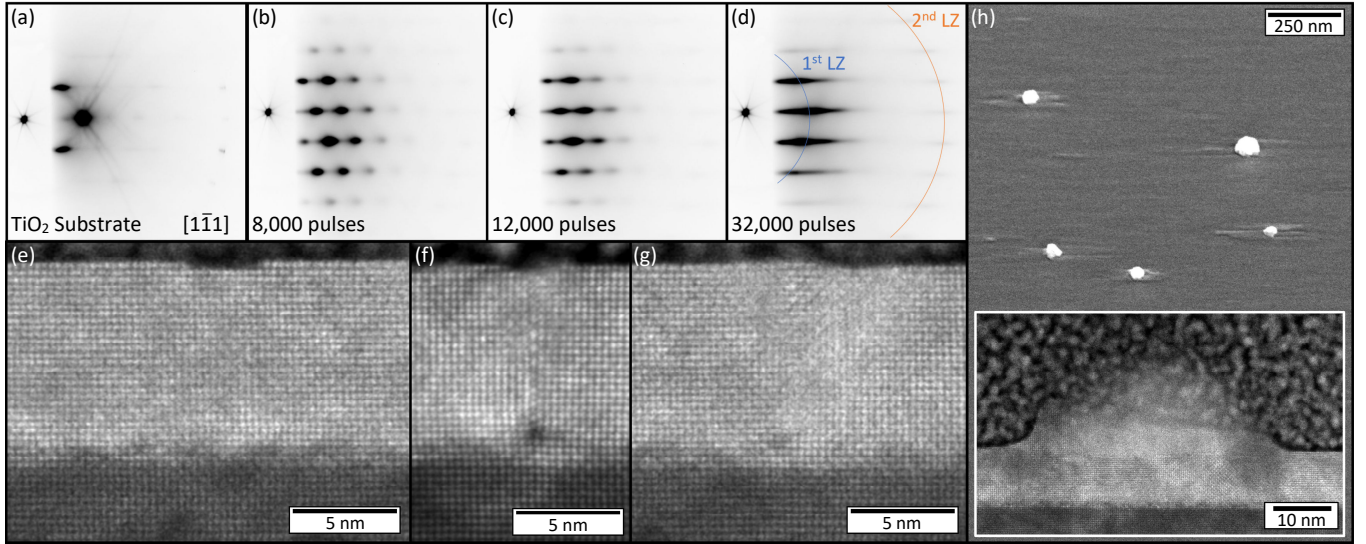


FIG. 4. Characterization of the island merging mechanism in RuO_2 . RHEED images of (a) the clean TiO_2 substrate, (b) the RuO_2 islands after 8,000 pulses, (c) the RuO_2 islands merging after 12,000 pulses and (d) the closed RuO_2 film after 32,000 pulses. The 1st and 2nd order Laue zones (LZ) are marked in blue and orange. STEM measurements of single-crystalline film section (e) without defects, (f) with edge dislocation that compensates the lattice mismatch and (g) with disorder in the island merging zone. (h) SEM image show a flat RuO_2 surface with occasional RuO_2 clusters on top. The inset is a STEM cross-section through one of these clusters.

the stoichiometry of the RuO_2 films, as indicated by the slight high energy shift of the Ru 3d XPS core level spectra of Fig. 3 (b,c). We speculate a reduced removal of oxygen from the target at lower laser energy densities to cause this slight reduction in metallicity, i.e., core level screening.

IV. EPITAXIAL FILM GROWTH OF RuO_2

A. Island merging in RuO_2

As demonstrated by He et al. via PVD,¹ one possible method to grow closed epitaxial thin films of RuO_2 on TiO_2 substrates is through island merging. Here we show that this growth mode can also be realized by PLD of RuO_2 . The individual phases of the growth process are visualized by RHEED in Fig. 4 (a)-(d). Starting from a $\text{TiO}_2(110)$ substrate that was prepared according to the protocol of Sec. III A in Fig. 4 (a) (corresponding AFM in Fig. 1), initial material deposi-

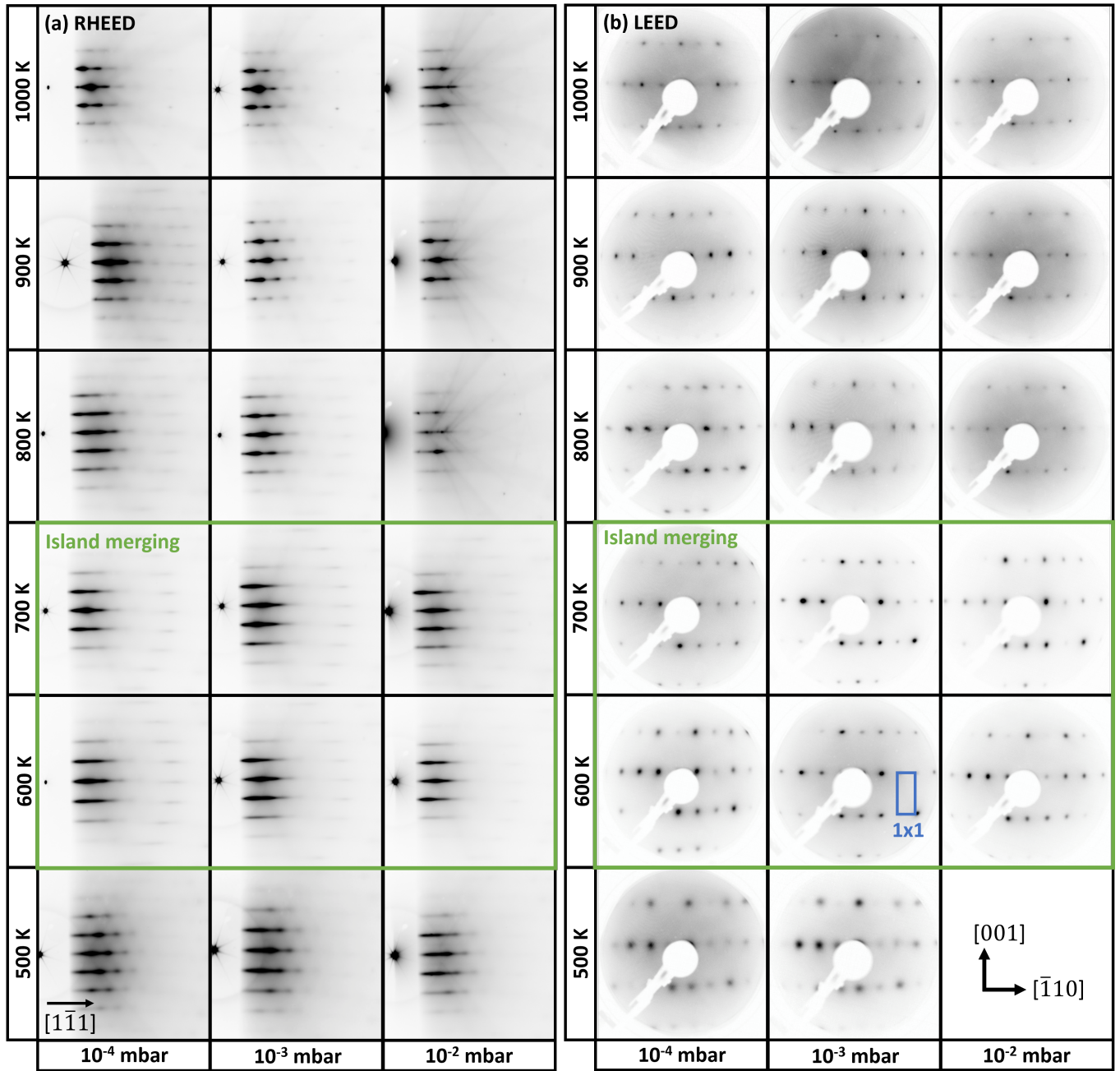


FIG. 5. (a) RHEED and (b) LEED images of as-grown RuO_2 films showing the influence of substrate temperature and oxygen partial pressure on surface crystallinity. The optimal temperature/pressure regime where island merging can be realized is marked in green. At 500 K and 1×10^{-2} mbar, no LEED was measured due to setup maintenance.

tion up to about 8,000 laser pulses results in the formation of islands, as visualized by the stripy RHEED pattern with distinct 3D transmission spots in Fig. 4 (b). Further deposition of material results in the coalition of these islands, indicated by a transition of the 3D transmission spots into a modulated streak pattern at 12,000 laser pulses (Fig. 4 (c)). After 32,000 laser pulses, the intensity modulations disappear and RHEED in Fig. 4 (d) displays the characteristic streak pattern of a closed film along with higher order diffraction spots in the

second Laue zone.¹⁰⁵ Indeed, exemplary STEM (Figs. 4 (e)-(g)) and SEM (Figs. 4 (h)) suggest a low surface corrugation of the final film on the order of only a few atoms, and a flat surface without trenches or residual islands, with occasional surface clusters (Fig. 4 (h) inset) that result from the deposition process. The STEM images of Fig. 4 (f) and (g), however, also reveal the drawback of this growth mode: In the merging zone of the initial islands, the compensation of the lattice mismatch leads to the formation of line defects (Fig. 4 (f)) and

disordered patches in the crystal lattice (Fig. 4 (g)).

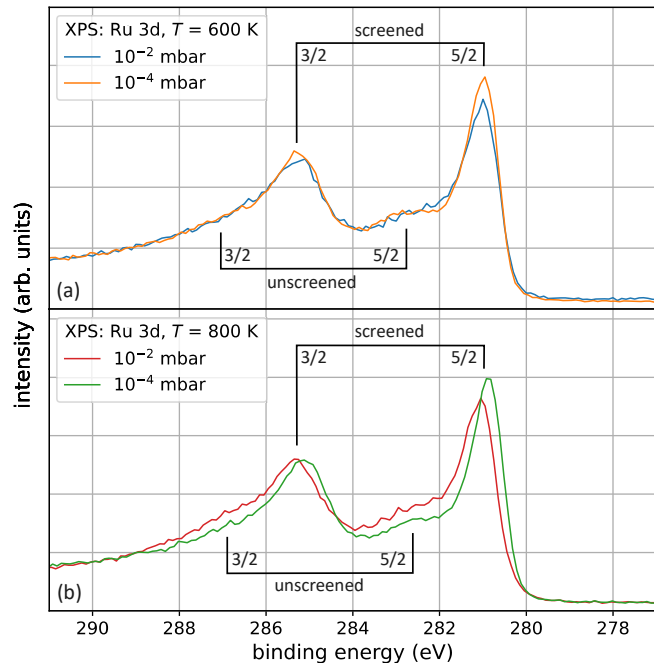


FIG. 6. Ru 3d core level spectra measured by XPS for RuO₂ films grown with different oxygen partial pressures at (a) 600 K and (b) 800 K, respectively.

B. Temperature and pressure dependent RuO₂ nucleation

Having outlined how to achieve closed epitaxial RuO₂ films via island merging, we now systematically study the influence of oxygen partial pressure and substrate temperature on RuO₂ growth in a wide parameter range from 1×10^{-4} mbar to 1×10^{-2} mbar and 500 K to 1000 K. All samples in this section were produced by applying a total of 16,000 laser pulses subject to the previously defined laser energy density gradient (Sec. III C) on two fresh 37.5 mm² RuO₂ target patches. The growth order was disarrayed, i.e., samples located next to each other in the growth parameter space were not grown consecutively. In this way, we were able to distinguish intrinsic trends from systematic errors, introduced, e.g., by a proceeding metallization of the laser entry window, a changing material flux or other similar factors. The RHEED and LEED images of the as-grown films are displayed in Fig. 5 (a) and (b), respectively.

Substrate temperatures of 600 K and 700 K result in the island merging growth mode as discussed in Sec. IV A irrespective of the oxygen partial pressure. RHEED in this temperature range (green) indicates the characteristic signature of a closed film with a streaked diffraction pattern and no transmission spots (Fig. 5 (a)), while LEED shows sharp diffraction spots and a low background intensity, indicating relatively high surface order (Fig. 5 (b)).

Increasing the substrate temperature to 800-1000 K increases the mobility of the deposited material, resulting in is-

land formation and a trenched surface. RHEED in Fig. 5 (a) now exhibits 3D transmission spots, while LEED in Fig. 5 (b) exhibits increased background intensity indicating an increased density of surface defects. In contrast, the diffraction spots are generally still sharp, suggesting the island terraces to still order locally.

Decreasing the substrate temperature to 500 K lowers the kinetic energy of the deposited material and again fosters island formation, yet suppresses the capability of island merging and a subsequent step-flow growth mode. RHEED in Fig. 5 now again shows the characteristic 3D transmission spots, while LEED in Fig. 5 (b) shows high background intensity and broad diffraction peaks indicative of disordered island terraces.

While the RHEED and LEED signatures of Figs. 5 (a) and (b) indicate the growth mode to be predominantly impacted by temperature, the oxygen partial pressure mostly influences the number and density of defects. Thus, while the augmented streakiness of RHEED patterns at higher O₂ pressure in Fig. 5 (a) reveals flatter films, corresponding LEED images in Fig. 5 (b) tend towards sharper spots, less overall background intensity and consequently higher surface order. We attribute this to an improved (surface) stoichiometry rationalized by the XPS in Fig. 6: Irrespective of the growth temperature, the ratio between the unscreened (i.e. oxidized) and the screened (i.e. metallic) Ru 3d core level peaks increases for higher O₂ pressure, suggesting a reduced amount of oxygen deficiencies.¹⁰⁶ However, we overall observe a lower material deposition rate at higher oxygen partial pressures, which is likely a result of Ru and RuO₂ over-oxidation to volatile RuO₄.¹⁰⁷

C. Characteristic thicknesses of RuO₂

As discussed above, RuO₂ films grown at substrate temperatures above 700 K show a trenched surface morphology, likely related by the interplay of augmented material diffusion, surface- and volume energies as well as substrate induced strain. While exemplary SEM and STEM images in Fig. 7 show these trenches to be randomly distributed across the sample and to not orient along preferred crystal directions, the remaining film still terminates in a flat and well defined fashion. In particular, the STEM images show the appearance of characteristic film thicknesses, namely 6 uc (blue), 20 uc (red) and 43 uc (green) as marked by the colored horizontal lines in Figs. 7 (b) and (c). As these exact thicknesses were found repeatedly irrespective of the sample or sample location, they seem to reflect a universal property of the RuO₂/TiO₂(110) interface. While we are not aware of reports of such a growth behaviour in literature, we would still like to point out certain similarities to results presented in Refs. 108–111.

We speculate that this tendency of RuO₂ to form islands of fixed thicknesses might directly compete with the tendency of RuO₂ to release lattice strain by forming islands that eventually coalesce and merge. The former mechanism would thus become more prevalent at higher growth temperatures, where surface diffusion is enhanced. This interpretation might be the

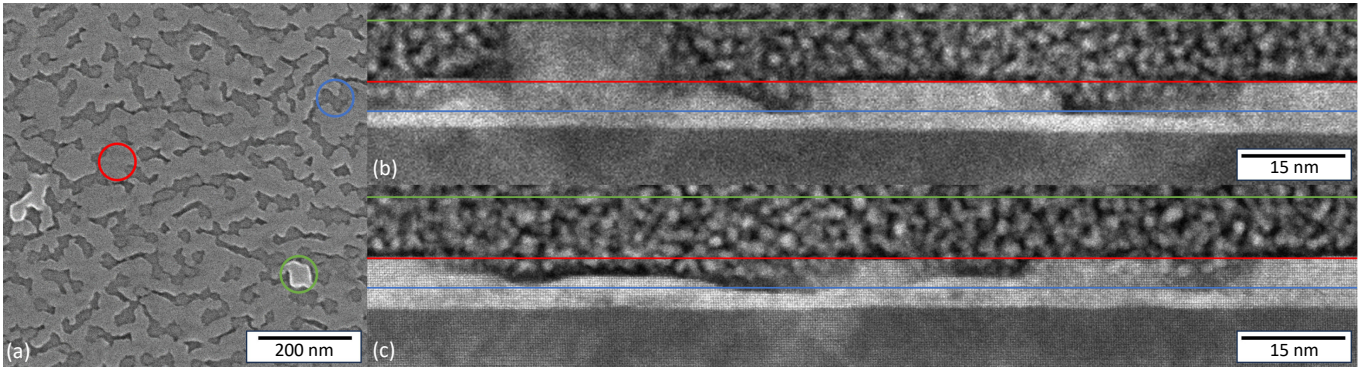


FIG. 7. Trenched surface morphology of RuO_2 films grown above 700 K. (a) SEM image showing the trench structure and two marked regions of characteristic film thicknesses. (b,c) STEM images taken at two laterally separated parts of one sample, exhibiting three characteristic RuO_2 film thicknesses of 6 uc (blue), 20 uc (red) and 43 uc (green).

reason why above 700 K, island merging of RuO_2 could not be observed and uniformly thick closed films were unachievable.

D. Layer-by-layer growth of RuO_2

Finally, we studied a growth regime where $\text{RuO}_2(110)$ on $\text{TiO}_2(110)$ grows layer-by-layer, allowing for the growth of closed, fully strained films up to 2 nm thickness. This growth process is achieved if surface diffusion is greatly reduced, i.e., if the RuO_2 material flux is massively increased during the nucleation phase (laser energy density: 2.4 J/cm^2 , pre-ablation: 2,000 pulses, oxygen partial pressure: 1×10^{-3} mbar, substrate temperature: 700 K). As seen in Fig. 8 (a), we now observe RHEED intensity oscillations and a transmission spot free diffraction pattern up to the 5th layer at this laser energy density. A continuation of the growth leads to a sharp drop in the RHEED intensity, accompanied by the appearance of 3D transmission spots resulting from island growth taking over in Fig. 8 (b).

V. EPITAXIAL FILM GROWTH OF IrO_2

A. Temperature and pressure dependent IrO_2 nucleation

As the 6.8% lattice mismatch between $\text{IrO}_2(110)$ and $\text{TiO}_2(110)$ along the $[00\bar{1}]$ direction is considerably larger than the 4.9% between $\text{RuO}_2(110)$ and $\text{TiO}_2(110)$,¹⁵ the tendency of IrO_2 to form islands and disorder is more pronounced than for RuO_2 . Further, while RuO_2 samples grown by PLD are essentially stoichiometric throughout all growth parameter regimes investigated in this study, IrO_2 films grown under similar conditions always contain considerable amounts of un- or underoxidized iridium, a consequence of its more 'stubborn' oxidation behaviour as compared to ruthenium.⁵⁰

To cope with these differences between the PLD growth of RuO_2 and IrO_2 and to better understand and control the nucleation phase of IrO_2 on $\text{TiO}_2(110)$, we employed a stopping criterion that allows for an objective comparison of IrO_2

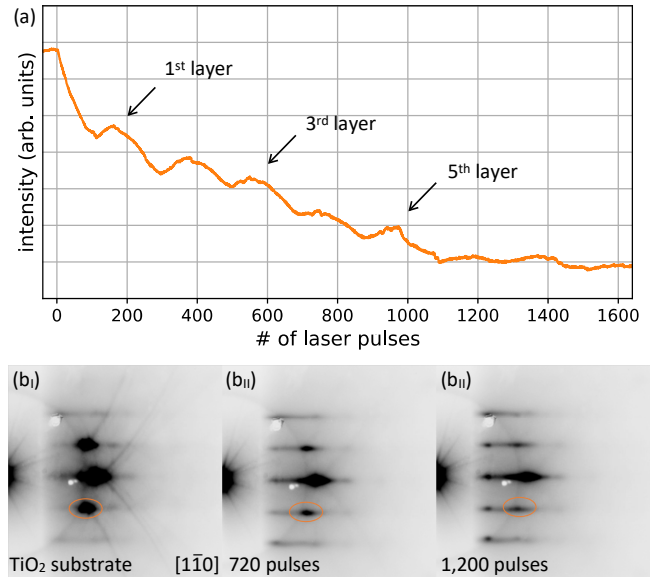


FIG. 8. Layer-by-layer growth of RuO_2 . (a) RHEED oscillations can be observed up to the 5th layer. (b) RHEED of the substrate (b_I), during Layer-by-layer growth (b_{II}) and after the formation of islands (b_{III}). The integration region for RHEED oscillations in (a) is marked in orange.

films grown at different substrate temperatures and oxygen partial pressures. This stopping criterion was reached once the intensity of a newly developed RHEED feature, such as a diffraction spot or a diffraction streak, surpassed 5% of the brightest initial substrate feature. The RHEED patterns of IrO_2 films grown systematically at oxygen partial pressures between 1×10^{-4} mbar and 1×10^{-2} mbar, substrate temperatures between 670 K and 870 K, and a laser energy density of 1.1 J/cm^2 are shown in Fig. 9. Like with RuO_2 , The growth order of IrO_2 films was disarrayed to avoid confusing intrinsic trends in the growth parameter space with systematic errors.

To further check for reproducibility of our results, we repeated the sample growth exemplarily at parameters 5×10^{-4} mbar / 870 K, 1×10^{-4} mbar / 770 K and 5×10^{-4} mbar

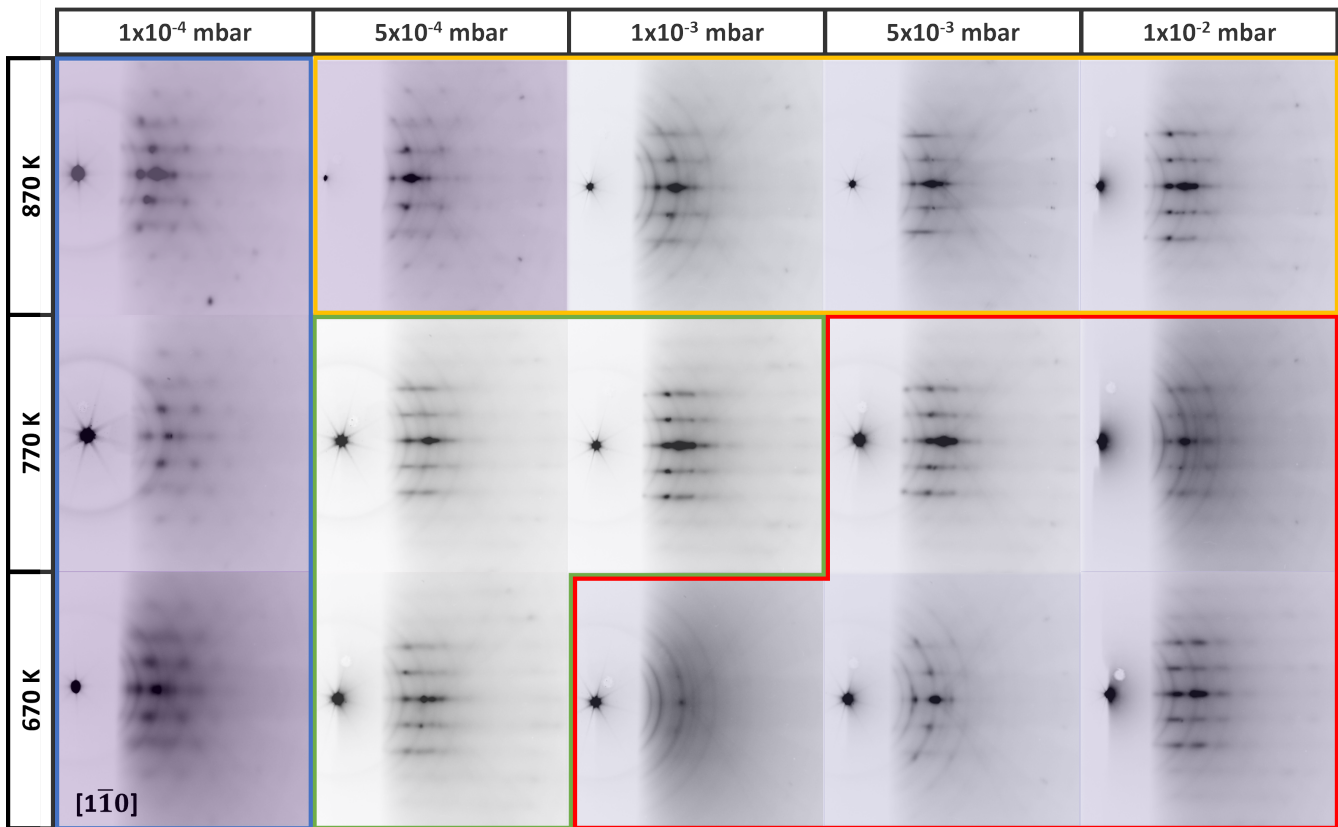


FIG. 9. Dependence of film quality on substrate temperature and oxygen partial pressure during growth. Shown are RHEED images of as-grown IrO_2 films terminated according to the stopping criterion defined in the main text. The Ir/IrO_2 ratio of these films as determined from the spectral decomposition of the Ir 4f peak according to Fig. 10 was used to color code the respective RHEED panels, where a dark blue represents high Ir/IrO_2 ratio (i.e., non-stoichiometric IrO_2 films with a high Ir concentration) and a light blue shading represents a low Ir/IrO_2 ratio (i.e., close to stoichiometric IrO_2 films with a low Ir concentration). The individual growth categories discussed in the text are marked by colored frames.

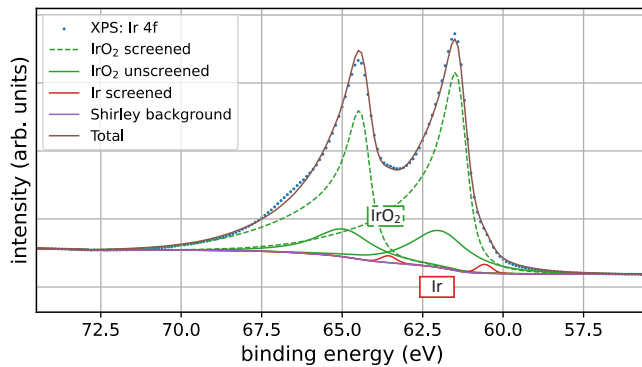


FIG. 10. Decomposition of an exemplary Ir 4f spectrum into IrO_2 and metallic Ir contributions. To determine the Ir/IrO_2 ratio, these spectra were corrected for the transmission function of the electron spectrometer and a Shirley background was subtracted.

/ 770 K, each yielding identical outcomes as compared to the first attempt. To benchmark the growth parameters with respect to the ‘stubborn’ oxidation behaviour of Ir, we used XPS

to determine the Ir/IrO_2 ratio of every film. Hereby, the corresponding Ir 4f core-level spectra were decomposed as exemplified in Fig. 10. After subtraction of a Shirley background and assuming a fixed intensity ratio of 4:3, the two Ir^{4+} 4f 7/2 and 5/2 peaks were fitted to asymmetric Voigt-like line-shapes as provided by CasaXPS.^{112–114} The Ir/IrO_2 ratios obtained in this way were used to color code the respective RHEED images of Fig. 9.

In addition to monitoring the Ir/IrO_2 ratio, we also analyzed the individual RHEED pattern of every film and identified four qualitatively different growth regimes, marked by the frame color in Fig. 9: The first category is indicated in red and represents disordered IrO_2 films grown at high oxygen partial pressures and low substrate temperatures. In this regime, the kinetic energy of the laser ablated particles is diminished by collisions in the oxygen gas, and diffusion on the substrate surface is limited by temperature.^{115,116} The diffusion of the deposited material is thus insufficient to achieve overall crystalline ordering, resulting in a RHEED pattern that is a superposition of Debye rings and 3D transmission spots as a consequence of disordered growth and island formation.⁵⁰

The second category is marked in orange and represents

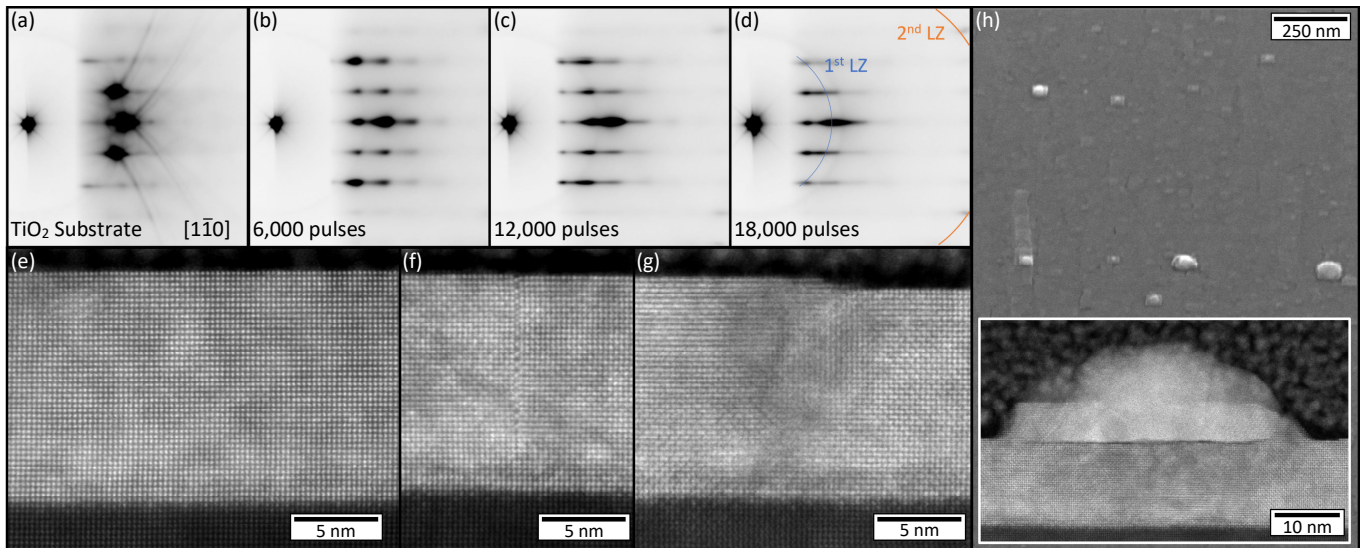


FIG. 11. Characterization of the island merging mechanism in IrO_2 . RHEED images of (a) the clean TiO_2 substrate, (b) the IrO_2 islands after 6,000 pulses, (c) the IrO_2 islands merging after 12,000 pulses and (d) the closed IrO_2 film after 18,000 pulses. The 1st and 2nd order Laue zones (LZ) are marked in blue and orange, respectively. STEM measurements of a single-crystalline film section (e) without defects, (f) with edge dislocation that compensates the lattice mismatch and (g) with disorder in the island merging zone. (h) SEM image showing a flat IrO_2 surface with occasional Ir clusters on top. The inset is a STEM cross-section through one of these clusters.

IrO_2 films grown at high substrate temperatures. This growth regime is characterized by a competition between the formation of higher, volatile oxides of iridium such as IrO_3 ,¹¹⁷ and the thermal reduction of IrO_2 to metallic Ir,¹¹⁸ which is controlled by the oxygen partial pressure. Thus, at high oxygen partial pressures, over-oxidation of metallic Ir as well as IrO_2 to volatile IrO_3 dominates.^{117,119–121} This limits the amount of deposited material and the growth rate, but keeps the Ir/ IrO_2 ratio generally low and yields a relatively well ordered, flat surface due to augmented surface diffusion. At lower oxygen partial pressures, the desorption rate of oxygen is enhanced and reduction of IrO_2 takes over,¹¹⁸ leading to disorder and island growth reflected in 3D transmission spots in RHEED and the highest Ir/ IrO_2 ratio within the explored parameters space.

This region overlaps with the third growth regime that is marked in blue and represents IrO_2 films grown at the lowest oxygen partial pressure. In contrast to the orange category, these samples exhibit a hexagonal RHEED pattern, i.e., a superposition of Debye rings and 3D transmission spots, indicating polycrystalline growth and island formation. Due to the lack of oxygen, oxidation of the deposited material is limited, leading to Ir/ IrO_2 ratios well beyond 15 % at high temperatures.

The best film quality was achieved for films within the green category, i.e., films grown at moderate substrate temperatures and oxygen partial pressures, where oxidation and surface diffusion are balanced out. RHEED displays a streaky pattern indicating relatively flat films, while XPS shows that these are essentially stoichiometric with Ir/ IrO_2 ratios below 5 %.

B. Island merging in IrO_2

The last section has shown that the optimal growth parameter set to achieve flat epitaxial IrO_2 films of appreciable thickness requires a fine balance between diffusion of the deposited material, Ir (over-)oxidation and IrO_2 reduction. In particular, while the sample stoichiometry is generally better for higher oxygen partial pressures, film deposition rate and hence thickness is limited due to the formation of volatile IrO_3 . As optimal parameter set, a temperature of 770 K and an oxygen partial pressure of 5×10^{-4} mbar was found, which lends itself as an ideal starting point to initiate the growth of closed IrO_2 thin films.

As shown in Fig. 11 and similar to what was observed for PLD and PVD¹ of RuO_2 , RHEED shows an initially pristine TiO_2 substrate (a) followed by the formation of islands with 3D transmission spots (b), which eventually coalesce (c) to form a closed, smooth film (d). Like for RuO_2 , high resolution STEM measurements in Fig. 11 (e) reveal a well defined surface termination, with occasional line defects to cope with strain as seen in (f), and with an increased amount of disorder close to the merging zone as shown in (g). An SEM image in Fig. 11 (h) further show a flat surface with tiny trenches, interrupted by occasional sprinkles and larger clusters of Ir, for which a STEM cross-section is shown in the inset.

Consistent with the local structural information by STEM in Fig. 11 (e-g), the Kiessig fringes in the XRR and the Laue-oscillations in the XRD data of Fig. 12 (b) and (c) suggests an excellent crystalline quality and morphology across the entire film. Analyzing their periodicity, we find an average thickness of 13 nm in good agreement with STEM. The XRD overview in Fig. 12 (a) further reveals an unwanted partial film cov-

erage with metallic iridium, consistent with our XPS study above and SEM and STEM images in Fig. 11 (h), both suggesting that iridium clusters are mostly located at the surface. In contrast, two peaks at 73.2° and 75.1° remain unidentified. Quite notably, however, both the iridium as well as the unidentified peaks disappear after the sample is annealed for 90 min at 450°C with an oxygen flow of 25 l/h (Fig. 12 (a)).

Finally, let us turn to nano electron diffraction data obtained from STEM on the 13 nm thick film of Fig. 12 (d), showing an overall well defined film-substrate-interface. A close-up of the (040) diffraction spot in panel (e) shows a lateral offset between the IrO_2 and TiO_2 peaks, indicating a partial relaxation of the IrO_2 film. Note that higher order diffraction further gives rise to otherwise forbidden peaks marked by the yellow circles in Fig. 12 (d).

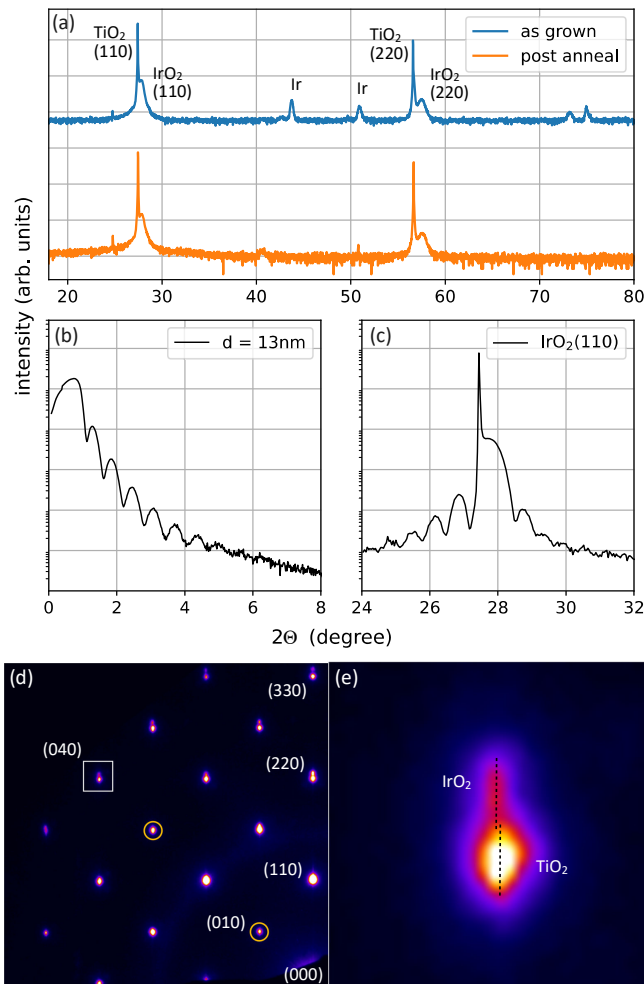


FIG. 12. Characterization of an IrO_2 film after island merging. (a) Overview XRD scan showing the presence of an Ir phase in addition to the $\text{IrO}_2(110)$ film. The Ir phase disappears after annealing the sample for 90 min at 450°C in oxygen. (b) XRR data and (c) Laue oscillations around the $\text{IrO}_2(110)$ diffraction peak yield a film thickness of 13 nm. (d) Nano electron diffraction data obtained from STEM indicates a good crystalline order. (e) The slight lateral offset of the IrO_2 vs the TiO_2 substrate (040) peak reveals the film to be partially relaxed.

VI. SUMMARY AND CONCLUSION

In summary, we systematically investigated the PLD growth of epitaxial $\text{RuO}_2(110)$ and $\text{IrO}_2(110)$ films on $\text{TiO}_2(110)$ substrates for a variety of substrate temperatures and oxygen partial pressures. By applying a temporal laser energy density gradient, we accounted for a decreasing material flux as a consequence of deteriorating target absorbance and an increasing coverage of the laser entry window. We find the film crystallinity and stoichiometry of RuO_2 to depend only mildly on the oxygen partial pressure during growth, which we varied in the range between 1×10^{-2} mbar to 1×10^{-4} mbar, with the growth rate being significantly reduced at higher pressures. The film quality, however, depends sensitively on substrate temperature. Low surface diffusion below 500 K leads to a disordered surface and the formation of volatile RuO_4 above 800 K promoting the formation of RuO_2 islands. The best surface quality was found for temperatures between 600 K and 700 K, yielding layer-by-layer growth of up to 5 unit cells and fully strained films for high deposition rates, and thicker, closed films through island merging at low deposition rates.

In contrast to RuO_2 , the IrO_2 film growth shows a pronounced dependence on both substrate temperature and oxygen partial pressure. We attribute this to the stronger resilience of Ir against oxidation and the tendency of IrO_2 to overoxidize to volatile IrO_3 . Growth rates thus are generally lower than for RuO_2 and samples tend to exhibit considerable fractions of metallic iridium, the latter can be removed by oxygen post annealing. Minimal amounts of metallic Ir contents have been achieved at oxygen pressures of around 5×10^{-4} mbar and temperatures around 770 K. In this setting, the initial island formation turns into a phase where the islands coalesce to form a closed, flat film.

ACKNOWLEDGMENTS

We thank Hiroshi Kumigashira for supplying us with the initial RuO_2 target. Funding support came from the Deutsche Forschungsgemeinschaft (DFG, German Research Foundation) under Germany's Excellence Strategy through the Würzburg-Dresden Cluster of Excellence on Complexity and Topology in Quantum Matter ct.qmat (EXC 2147, Project ID 390858490) and through the Collaborative Research Center SFB 1170 ToCoTronics (Project ID 258499086), as well as from the New Zealand Ministry of Business, Innovation and Employment (MBIE, Grant number: C05X2004).

The following article has been submitted to APL Materials. After it is published, it will be found at AIP Publishing

¹Y. He, D. Langsdorf, L. Li, and H. Over, "Versatile model system for studying processes ranging from heterogeneous to photocatalysis: Epitaxial $\text{RuO}_2(110)$ on $\text{TiO}_2(110)$," *Journal of Physical Chemistry C* **119**, 2692–2702 (2015).

²H. Over, "Surface Chemistry of Ruthenium Dioxide in Heterogeneous Catalysis and Electrocatalysis: From Fundamental to Applied Research," *Chemical Reviews* **112**, 3356–3426 (2012).

³J. F. Weaver, "Surface Chemistry of Late Transition Metal Oxides," *Chemical Reviews* **113**, 4164–4215 (2013).

- ⁴F. Scarpelli, N. Godbert, A. Crispini, and I. Aiello, "Nanostructured Iridium Oxide: State of the Art," *Inorganics* **10**, 115 (2022).
- ⁵H. Jang and J. Lee, "Iridium oxide fabrication and application: A review," *Journal of Energy Chemistry* **46**, 152–172 (2020).
- ⁶C. Spöri, J. T. H. Kwan, A. Bonakdarpour, D. P. Wilkinson, and P. Strasser, "Stabilitätsanforderungen von Elektrokatalysatoren für die Sauerstoffentwicklung: der Weg zu einem grundlegenden Verständnis und zur Minimierung der Katalysatordegradation," *Angewandte Chemie* **129**, 6088–6117 (2017).
- ⁷T. Weber, V. Vonk, M. J. Abb, J. Evertsson, A. Stierle, E. Lundgren, and H. Over, "In Situ Synchrotron-Based Studies of IrO₂(110)-TiO₂(110) under Harsh Acidic Water Splitting Conditions: Anodic Stability and Radiation Damages," *Journal of Physical Chemistry C* **126**, 20243–20250 (2022).
- ⁸T. Naito, T. Shinagawa, T. Nishimoto, and K. Takanabe, "Recent advances in understanding oxygen evolution reaction mechanisms over iridium oxide," *Inorganic Chemistry Frontiers* **8**, 2900–2917 (2021).
- ⁹F. Hess and H. Over, "Coordination Inversion of the Tetrahedrally Coordinated Ru4f Surface Complex on RuO₂(100) and Its Decisive Role in the Anodic Corrosion Process," *ACS Catalysis* **13**, 3433–3443 (2023).
- ¹⁰J. Abmann, D. Crihan, M. Knapp, E. Lundgren, E. Löffler, M. Muhler, V. Narkhede, H. Over, M. Schmid, A. P. Seitsonen, and P. Varga, "Understanding the structural deactivation of ruthenium catalysts on an atomic scale under both oxidizing and reducing conditions," *Angewandte Chemie - International Edition* **44**, 917–920 (2005).
- ¹¹K. A. Stoerzinger, L. Qiao, M. D. Biegalski, and Y. Shao-Horn, "Orientation-dependent oxygen evolution activities of rutile IrO₂ and RuO₂," *Journal of Physical Chemistry Letters* **5**, 1636–1641 (2014).
- ¹²S. Moser, V. Jovic, A. Consiglio, K. E. Smith, C. Jozwiak, A. Bostwick, E. Rotenberg, and D. Di Sante, "Momentum for catalysis: How surface reactions shape the RuO₂ flat surface state," *ACS Catalysis* , 1749–1757 (2021).
- ¹³C. Reiser, P. Keßler, M. Kamp, V. Jovic, and S. Moser, "Specific Capacitance of RuO₂ (110) Depends Sensitive on Surface Order," *The Journal of Physical Chemistry C* **2** (2023), 10.1021/acs.jpcc.2c07217.
- ¹⁴K. Seki, "Development of RuO₂/Rutile-TiO₂ Catalyst for Industrial HCl Oxidation Process," *Catalysis Surveys from Asia* **14**, 168–175 (2010).
- ¹⁵A. Jain, S. P. Ong, G. Hautier, W. Chen, W. D. Richards, S. Dacek, S. Cholia, D. Gunter, D. Skinner, G. Ceder, and K. A. Persson, "Commentary: The materials project: A materials genome approach to accelerating materials innovation," *APL Materials* **1** (2013), 10.1063/1.4812323.
- ¹⁶M. Uchida, T. Nomoto, M. Musashi, R. Arita, and M. Kawasaki, "Superconductivity in Uniquely Strained RuO₂ Films," *Physical Review Letters* **125** (2020), 10.1103/PhysRevLett.125.147001.
- ¹⁷J. P. Ruf, H. Paik, N. J. Schreiber, H. P. Nair, L. Miao, J. K. Kawasaki, J. N. Nelson, B. D. Faeth, Y. Lee, B. H. Goodge, B. Pamuk, C. J. Fennie, L. F. Kourkoutis, D. G. Schlom, and K. M. Shen, "Strain-stabilized superconductivity," *Nature Communications* **12**, 1–8 (2021).
- ¹⁸G. Bai, I.-f. Tsu, A. Wang, and C. M. Foster, "By Low-Temperature Metal – Organic Chemical Vapor Deposition," *Applied Physics Letters* **72**, 1572–1574 (1998).
- ¹⁹L. Mattheiss, "Electronic structure of RuO₂, OsO₂, and IrO₂," *Physical Review B* **13**, 2433–2450 (1976).
- ²⁰V. Jovic, R. J. Koch, S. K. Panda, H. Berger, P. Bugnon, A. Magrez, K. E. Smith, S. Biermann, C. Jozwiak, A. Bostwick, E. Rotenberg, and S. Moser, "Dirac nodal lines and flat-band surface state in the functional oxide RuO₂," *Physical Review B* **98**, 241101 (2018).
- ²¹V. Jovic, R. J. Koch, S. K. Panda, H. Berger, P. Bugnon, A. Magrez, R. Thomale, K. E. Smith, S. Biermann, C. Jozwiak, A. Bostwick, E. Rotenberg, D. Di Sante, and S. Moser, "The Dirac nodal line network in non-symmorphic rutile semimetal RuO₂," *cond-mat.mes-hall* (2019), arXiv:1908.02621.
- ²²Y. Sun, Y. Zhang, C.-X. Liu, C. Felser, and B. Yan, "Dirac nodal lines and induced spin Hall effect in metallic rutile oxides," *Physical Review B* **95**, 235104 (2017), 1701.09089.
- ²³K.-H. Ahn, A. Hariki, K.-W. Lee, and J. Kuneš, "Antiferromagnetism in RuO₂ as d-wave Pomeranchuk instability," *Physical Review B* **99**, 184432 (2019).
- ²⁴T. Berlijn, P. C. Snijders, O. Delaire, H.-D. Zhou, T. A. Maier, H.-B. Cao, S.-X. Chi, M. Matsuda, Y. Wang, M. R. Koehler, P. R. C. Kent, and H. H. Weitering, "Itinerant Antiferromagnetism in RuO₂," *Physical Review Letters* **118**, 077201 (2017).
- ²⁵Z. H. Zhu, J. Stremper, R. R. Rao, C. A. Occhialini, J. Pelliciani, Y. Choi, T. Kawaguchi, H. You, J. F. Mitchell, Y. Shao-Horn, and R. Comin, "Anomalous Antiferromagnetism in Metallic RuO₂ Determined by Resonant X-ray Scattering," *Physical Review Letters* **122** (2019), 10.1103/PhysRevLett.122.017202.
- ²⁶S. W. Lovesey, D. D. Khalyavin, and G. van der Laan, "Magnetic properties of ruthenium dioxide (RuO₂) and charge-magnetic interference in Bragg diffraction of circularly polarized x-rays," arxiv (2021).
- ²⁷M. Hiraishi, H. Okabe, A. Koda, R. Kadono, T. Muroi, D. Hirai, and Z. Hiroi, "Nonmagnetic Ground State in RuO₂ Revealed by Muon Spin Rotation," *Physical Review Letters* **132**, 166702 (2024).
- ²⁸P. Keßler, L. Garcia-Gassull, A. Suter, T. Prokscha, Z. Salman, D. Khalyavin, P. Manuel, F. Orlandi, I. I. Mazin, R. Valentí, and S. Moser, "Absence of magnetic order in RuO₂: insights from μ SR spectroscopy and neutron diffraction," , 1–12 (2024), arXiv:2405.10820.
- ²⁹H. Over, M. Knapp, E. Lundgren, A. P. Seitsonen, M. Schmid, and P. Varga, "Visualization of atomic processes on ruthenium dioxide using scanning tunneling microscopy," *ChemPhysChem* **5**, 167–174 (2004).
- ³⁰X. Fang, M. Tachiki, and T. Kobayashi, "Growth of RuO₂ Thin Films on a MgO Substrate by Pulsed Laser Deposition Method," *Japanese Journal of Applied Physics* **36**, L511–L514 (1997).
- ³¹X. Wang, A. F. Pun, Y. Xin, and J. P. Zheng, "Investigation of the growth dynamics of pulsed laser-deposited RuO₂ films using in situ resistance measurement and atomic force microscopy," *Thin Solid Films* **510**, 82–87 (2006).
- ³²H. Kim, N. A. Charipar, J. Figueroa, N. S. Bingham, and A. Piqué, "Control of metal-insulator transition temperature in VO₂ thin films grown on RuO₂/TiO₂ templates by strain modification," *AIP Advances* **9** (2019), 10.1063/1.5083848.
- ³³Z. Feng, X. Zhou, L. Šmejkal, L. Wu, Z. Zhu, H. Guo, R. González-Hernández, X. Wang, H. Yan, P. Qin, X. Zhang, H. Wu, H. Chen, Z. Meng, L. Liu, Z. Xia, J. Sinova, T. Jungwirth, and Z. Liu, "An anomalous Hall effect in altermagnetic ruthenium dioxide," *Nature Electronics* **5**, 735–743 (2022).
- ³⁴T. Tschirner, P. Keßler, R. D. G. Betancourt, T. Kotte, D. Krieger, B. Büchner, J. Dufouleur, M. Kamp, V. Jovic, L. Šmejkal, J. Sinova, R. Claessen, T. Jungwirth, S. Moser, H. Reichlova, and L. Veyrat, "Saturation of the anomalous Hall effect at high magnetic fields in altermagnetic RuO₂," *APL Materials* **11** (2023), 10.1063/5.0160335.
- ³⁵A. Bose, N. J. Schreiber, R. Jain, D. F. Shao, H. P. Nair, J. Sun, X. S. Zhang, D. A. Muller, E. Y. Tsybmal, D. G. Schlom, and D. C. Ralph, "Tilted spin current generated by the collinear antiferromagnet ruthenium dioxide," *Nature Electronics* **5**, 267–274 (2022).
- ³⁶D.-F. Shao, S.-H. Zhang, M. Li, C.-B. Eom, and E. Y. Tsybmal, "Spin-neutral currents for spintronics," *Nature Communications* **12**, 7061 (2021), 2103.09219.
- ³⁷L. Šmejkal, J. Sinova, and T. Jungwirth, "Beyond Conventional Ferromagnetism and Antiferromagnetism: A Phase with Nonrelativistic Spin and Crystal Rotation Symmetry," *Physical Review X* **12**, 031042 (2022).
- ³⁸L. Šmejkal, J. Sinova, and T. Jungwirth, "Emerging Research Landscape of Altermagnetism," *Physical Review X* **12**, 1–27 (2022), 2204.10844.
- ³⁹J. N. Nelson, J. P. Ruf, Y. Lee, C. Zeledon, J. K. Kawasaki, S. Moser, C. Jozwiak, E. Rotenberg, A. Bostwick, D. G. Schlom, K. M. Shen, and L. Moreschini, "Dirac nodal lines protected against spin-orbit interaction in IrO₂," *Physical Review Materials* **3**, 64205 (2019).
- ⁴⁰A. Bose, J. N. Nelson, X. S. Zhang, P. Jadaun, R. Jain, D. G. Schlom, D. C. Ralph, D. A. Muller, K. M. Shen, and R. A. Buhrman, "Effects of Anisotropic Strain on Spin-Orbit Torque Produced by the Dirac Nodal Line Semimetal IrO₂," *ACS Applied Materials and Interfaces* **12**, 55411–55416 (2020).
- ⁴¹M. Patton, G. Gurung, D. F. Shao, G. Noh, J. A. Mittelstaedt, M. Mazur, J. W. Kim, P. J. Ryan, E. Y. Tsybmal, S. Y. Choi, D. C. Ralph, M. S. Rzchowski, T. Nan, and C. B. Eom, "Symmetry Control of Unconventional Spin-Orbit Torques in IrO₂," *Advanced Materials* **35**, 1–8 (2023).
- ⁴²S. Gottesfeld, J. D. McIntyre, G. Beni, and J. L. Shay, "Electrochromism in anodic iridium oxide films," *Applied Physics Letters* **33**, 208–210 (1978).
- ⁴³P. S. Patil, R. K. Kwar, and S. B. Sadale, "Electrochromism in spray

- deposited iridium oxide thin films,” *Electrochimica Acta* **50**, 2527–2532 (2005).
- ⁴⁴K. Fujiwara, Y. Fukuma, J. Matsuno, H. Idzuchi, Y. Niimi, Y. Otani, and H. Takagi, “5d iridium oxide as a material for spin-current detection,” *Nature Communications* **4**, 2893 (2013).
- ⁴⁵M. Uchida, W. Sano, K. S. Takahashi, T. Koretsune, Y. Kozuka, R. Arita, Y. Tokura, and M. Kawasaki, “Field-direction control of the type of charge carriers in nonsymmorphic IrO₂,” *Physical Review B* **91**, 241119 (2015).
- ⁴⁶Y. Ping, G. Galli, and W. A. Goddard, “Electronic structure of IrO₂: The role of the metal d orbitals,” *Journal of Physical Chemistry C* **119**, 11570–11577 (2015).
- ⁴⁷L. W. Martin, J.-P. Maria, and D. G. Schlom, “Lifting the fog in ferroelectric thin-film synthesis,” *Nature Materials* **23**, 9–10 (2024).
- ⁴⁸Y. B. He, A. Stierle, W. X. Li, A. Farkas, N. Kasper, and H. Over, “Oxidation of Ir(111): From O-Ir-O trilayer to bulk oxide formation,” *Journal of Physical Chemistry C* **112**, 11946–11953 (2008).
- ⁴⁹W.-H. Chung, D.-S. Tsai, L.-J. Fan, Y.-W. Yang, and Y.-S. Huang, “Surface oxides of Ir(111) prepared by gas-phase oxygen atoms,” *Surface Science* **606**, 1965–1971 (2012).
- ⁵⁰S. Nair, Z. Yang, D. Lee, S. Guo, J. T. Sadowski, S. Johnson, A. Saboor, Y. Li, H. Zhou, R. B. Comes, W. Jin, K. A. Mkhoyan, A. Janotti, and B. Jalan, “Engineering metal oxidation using epitaxial strain,” *Nature Nanotechnology* (2023), 10.1038/s41565-023-01397-0.
- ⁵¹S. G. Bhat, A. M. Koshy, S. Pittala, and P. S. Kumar, “Tuning the growth of IrO₂ on SrTiO₃ (100) for spin-hall effect based oxide devices,” *AIP Conference Proceedings* **1859** (2017), 10.1063/1.4990160.
- ⁵²E. Arias-Egido, M. A. Laguna-Marco, C. Piquer, P. Jiménez-Cavero, I. Lucas, L. Morellón, F. Gallego, A. Rivera-Calzada, M. Cabero-Piris, J. Santamaria, G. Fabbris, D. Haskel, R. Boada, and S. Díaz-Moreno, “Dimensionality-driven metal-insulator transition in spin-orbit-coupled IrO₂,” *Nanoscale* **13**, 17125–17135 (2021).
- ⁵³M. J. Abb, B. Herd, and H. Over, “Template-Assisted Growth of Ultrathin Single-Crystalline IrO₂(110) Films on RuO₂(110)/Ru(0001) and Its Thermal Stability,” *Journal of Physical Chemistry C* **122**, 14725–14732 (2018).
- ⁵⁴B. Herd, M. Knapp, and H. Over, “Atomic scale insights into the initial oxidation of Ru(0001) using molecular oxygen: A scanning tunneling microscopy study,” *Journal of Physical Chemistry C* **116**, 24649–24660 (2012).
- ⁵⁵T. Weber, J. Pfrommer, M. J. Abb, B. Herd, O. Khalid, M. Rohnke, P. H. Lakner, J. Evertsson, S. Volkov, F. Bertram, R. Znaiguia, F. Carla, V. Vonk, E. Lundgren, A. Stierle, and H. Over, “Potential-Induced Pitting Corrosion of an IrO₂(110)-RuO₂(110)/Ru(0001) Model Electrode under Oxygen Evolution Reaction Conditions,” *ACS Catalysis* **9**, 6530–6539 (2019).
- ⁵⁶R. Rai, T. Li, Z. Liang, M. Kim, A. Asthagiri, and J. F. Weaver, “Growth and termination of a rutile IrO₂(100) layer on Ir(111),” *Surface Science* **652**, 213–221 (2016).
- ⁵⁷Z. Liang, T. Li, M. Kim, A. Asthagiri, and J. F. Weaver, “Low-temperature activation of methane on the IrO₂(110) surface,” *Science* **356**, 299–303 (2017).
- ⁵⁸Y. Kim, Y. Gao, and S. Chambers, “Core-level X-ray photoelectron spectra and X-ray photoelectron diffraction of RuO₂(110) grown by molecular beam epitaxy on TiO₂(110),” *Applied Surface Science* **120**, 250–260 (1997).
- ⁵⁹W. Nunn, S. Nair, H. Yun, A. K. Manjeshwar, A. Rajapitamahuni, D. Lee, K. A. Mkhoyan, and B. Jalan, “Solid-source metal-organic molecular beam epitaxy of epitaxial RuO₂,” *APL Materials* **9** (2021), 10.1063/5.0062726.
- ⁶⁰J. K. Kawasaki, D. Baek, H. Paik, H. P. Nair, L. F. Kourkoutis, D. G. Schlom, and K. M. Shen, “Rutile IrO₂/TiO₂ superlattices: A hyperconnected analog to the Ruddelsden-Popper structure,” *Physical Review Materials* **2** (2018), 10.1103/PhysRevMaterials.2.054206.
- ⁶¹J. K. Kawasaki, C. H. Kim, J. N. Nelson, S. Crisp, C. J. Zollner, E. Biegenwald, J. T. Heron, C. J. Fennie, D. G. Schlom, and K. M. Shen, “Engineering Carrier Effective Masses in Ultrathin Quantum Wells of IrO₂,” *Physical Review Letters* **121** (2018), 10.1103/PhysRevLett.121.176802.
- ⁶²J. K. Kawasaki, M. Uchida, H. Paik, D. G. Schlom, and K. M. Shen, “Evolution of electronic correlations across the rutile, perovskite, and Ruddelsden-Popper iridates with octahedral connectivity,” *Physical Review B* **94**, 121104 (2016).
- ⁶³D. Y. Kuo, H. Paik, J. N. Nelson, K. M. Shen, D. G. Schlom, and J. Sun-tivich, “Chlorine evolution reaction electrocatalysis on RuO₂ (110) and IrO₂ (110) grown using molecular-beam epitaxy,” *Journal of Chemical Physics* **150** (2019), 10.1063/1.5051429.
- ⁶⁴A. Iembo, F. Fuso, E. Arimondo, C. Ciofi, G. Pennelli, G. M. Currò, F. Neri, and M. Allegrini, “Pulsed laser deposition and characterization of conductive RuO₂ thin films,” *Journal of Materials Research* **12**, 1433–1436 (1997).
- ⁶⁵L. M. Zhang, Y. S. Gong, C. B. Wang, and Q. Shen, “Microstructure and Resistivity of Iridium Oxide Thin Films by Pulsed Laser Deposition Technique,” *Key Engineering Materials* **336-338**, 2215–2217 (2007).
- ⁶⁶M. El Khakani and M. Chaker, “Highly Conductive and Optically Transparent Polycrystalline Iridium Oxide Thin Films Grown by Reactive Pulsed Laser Deposition,” *MRS Proceedings* **472**, 373 (1997).
- ⁶⁷M. El Khakani and M. Chaker, “Reactive pulsed laser deposition of iridium oxide thin films,” *Thin Solid Films* **335**, 6–12 (1998).
- ⁶⁸M. A. El Khakani, M. Chaker, and E. Gat, “Pulsed laser deposition of highly conductive iridium oxide thin films,” *Applied Physics Letters* **69**, 2027–2029 (1996).
- ⁶⁹W. J. Kim, S. Y. Kim, C. H. Kim, C. H. Sohn, O. B. Korneta, S. C. Chae, and T. W. Noh, “Spin-orbit coupling induced band structure change and orbital character of epitaxial IrO₂ films,” *Physical Review B* **93**, 045104 (2016).
- ⁷⁰X. Hou, R. Takahashi, T. Yamamoto, and M. Lippmaa, “Microstructure analysis of IrO₂ thin films,” *Journal of Crystal Growth* **462**, 24–28 (2017).
- ⁷¹Q. Wang, W. L. Gladfelter, D. Fennell Evans, Y. Fan, and A. Franciosi, “Reactive-sputter deposition and structure of RuO₂ films on sapphire and strontium titanate,” *Journal of Vacuum Science & Technology A: Vacuum, Surfaces, and Films* **14**, 747–752 (1996).
- ⁷²J. Huang, “Material characteristics and electrical property of reactively sputtered RuO₂ thin films,” *Thin Solid Films* **382**, 139–145 (2001).
- ⁷³L. J. Meng and M. P. Dos Santos, “Characterization of RuO₂ films prepared by rf reactive magnetron sputtering,” *Applied Surface Science* **147**, 94–100 (1999).
- ⁷⁴E. A. Paoli, F. Masini, R. Frydendal, D. Deiana, C. Schlaup, M. Malizia, T. W. Hansen, S. Horch, I. E. L. Stephens, and I. Chorkendorff, “Oxygen evolution on well-characterized mass-selected Ru and RuO₂ nanoparticles,” *Chemical Science* **6**, 190–196 (2015).
- ⁷⁵Y. Liu, H. Bai, Y. Song, Z. Ji, S. Lou, Z. Zhang, C. Song, and Q. Jin, “Inverse Altermagnetic Spin Splitting Effect-Induced Terahertz Emission in RuO₂,” *Advanced Optical Materials* **11**, 1–7 (2023).
- ⁷⁶J. Klein, S. Clauson, and S. Cogan, “Reactive IrO₂ sputtering in reducing/oxidizing atmospheres,” *Journal of Materials Research* **10**, 328–333 (1995).
- ⁷⁷J. Klein, S. Clauson, and S. Cogan, “Reactive IrO₂ sputtering in reducing/oxidizing atmospheres,” *Journal of Materials Research* **10**, 328–333 (1995).
- ⁷⁸V. Balu, T.-S. Chen, B. Jiang, S.-H. Kuah, J. C. Lee, P. Chu, R. E. Jones, P. Zurcher, D. J. Taylor, and S. Gillespie, “Electrode Materials for Ferroelectric Capacitors: Properties of Reactive DC Sputtered IrO₂ Thin Films,” *MRS Proceedings* **433**, 139 (1996).
- ⁷⁹M. Shimizu, H. Fujisawa, S. Hyodo, S. Nakashima, H. Niu, H. Okino, and T. Shiosaki, “Effects of Sputtered Ir and IrO₂ Electrodes on the Properties of PZT Thin Films Deposited By MOCVD,” *MRS Proceedings* **493**, 159 (1997).
- ⁸⁰D.-Q. Liu, S.-H. Yu, S.-W. Son, and S.-K. Joo, “Supercapacitive Studies on IrO₂ Thin Film Electrodes Prepared by Radio Frequency Magnetron Sputtering,” *Electrochemical and Solid-State Letters* **11**, A206 (2008).
- ⁸¹A. van Ooyen, G. Topalov, G. Ganske, W. Mokwa, and U. Schnakenberg, “Iridium oxide deposited by pulsed dc-sputtering for stimulation electrodes,” *Journal of Micromechanics and Microengineering* **19**, 074009 (2009).
- ⁸²S. F. Cogan, J. Ehrlich, T. D. Plante, A. Smirnov, D. B. Shire, M. Gingerich, and J. F. Rizzo, “Sputtered iridium oxide films for neural stimulation electrodes,” *Journal of Biomedical Materials Research Part B: Applied Biomaterials* **89B**, 353–361 (2009).
- ⁸³J.-H. Kim, D.-S. Kil, S.-J. Yeom, J.-S. Roh, N.-J. Kwak, and J.-W. Kim, “Modified atomic layer deposition of RuO₂ thin films for capacitor electrodes,” *Applied Physics Letters* **91**, 1–4 (2007).
- ⁸⁴S.-H. Kwon, O.-K. Kwon, J.-H. Kim, S.-J. Jeong, S.-W. Kim, and S.-W.

- Kang, "Improvement of the Morphological Stability by Stacking RuO₂ on Ru Thin Films with Atomic Layer Deposition," *Journal of The Electrochemical Society* **154**, H773 (2007).
- ⁸⁵J.-Y. Park, S. Yeo, T. Cheon, S.-H. Kim, M.-K. Kim, H. Kim, T. E. Hong, and D.-J. Lee, "Growth of highly conformal ruthenium-oxide thin films with enhanced nucleation by atomic layer deposition," *Journal of Alloys and Compounds* **610**, 529–539 (2014).
- ⁸⁶H. J. Jung, J. H. Han, E. A. Jung, B. K. Park, J.-H. Hwang, S. U. Son, C. G. Kim, T.-m. Chung, and K.-s. An, "Atomic Layer Deposition of Ruthenium and Ruthenium Oxide Thin Films from a Zero-Valent (1,5-Hexadiene)(1-isopropyl-4-methylbenzene)ruthenium Complex and O₂," *Chemistry of Materials* **26**, 7083–7090 (2014), 10.1021/cm5035485 [dx.doi.org].
- ⁸⁷J. Hämäläinen, T. Hatanpää, E. Puukilainen, T. Sajavaara, M. Ritala, and M. Leskelä, "Iridium metal and iridium oxide thin films grown by atomic layer deposition at low temperatures," *Journal of Materials Chemistry* **21**, 16488 (2011).
- ⁸⁸M. Mattinen, J. Hämäläinen, F. Gao, P. Jalkanen, K. Mizohata, J. Räisänen, R. L. Puurunen, M. Ritala, and M. Leskelä, "Nucleation and Conformality of Iridium and Iridium Oxide Thin Films Grown by Atomic Layer Deposition," *Langmuir* **32**, 10559–10569 (2016).
- ⁸⁹S.-W. Kim, S.-H. Kwon, D.-K. Kwak, and S.-W. Kang, "Phase control of iridium and iridium oxide thin films in atomic layer deposition," *Journal of Applied Physics* **103**, 1–7 (2008).
- ⁹⁰J. Hämäläinen, M. Kemell, F. Munnik, U. Kreissig, M. Ritala, and M. Leskelä, "Atomic Layer Deposition of Iridium Oxide Thin Films from Ir(acac)₃ and Ozone," *Chemistry of Materials* **20**, 2903–2907 (2008).
- ⁹¹N. Simon, M. Asplund, T. Stieglitz, and V. Bucher, "Plasma Enhanced Atomic Layer Deposition of Iridium Oxide for Application in Miniaturized Neural Implants," *Current Directions in Biomedical Engineering* **7**, 539–542 (2021).
- ⁹²D. Y. Kim, J. Mannhart, and W. Braun, "Thermal laser evaporation for the growth of oxide films," *APL Materials* **9**, 081105 (2021).
- ⁹³M. Knapp, D. Crihan, A. P. Seitsonen, E. Lundgren, A. Resta, J. N. Andersen, and H. Over, "Complex interaction of hydrogen with the RuO₂(110) surface," *Journal of Physical Chemistry C* **111**, 5363–5373 (2007).
- ⁹⁴Y. D. Kim, A. P. Seitsonen, and H. Over, "Atomic geometry of oxygen-rich Ru(0001) surfaces: Coexistence of (1 × 1)O and RuO₂(110) domains," *Surface Science* **465**, 1–8 (2000).
- ⁹⁵J. Abmann, D. Crihan, M. Knapp, E. Lundgren, E. Löffler, M. Muhler, V. Narkhede, H. Over, M. Schmid, A. P. Seitsonen, and P. Varga, "Understanding the structural deactivation of ruthenium catalysts on an atomic scale under both oxidizing and reducing conditions," *Angewandte Chemie - International Edition* **44**, 917–920 (2005).
- ⁹⁶Q. X. Jia, X. D. Wu, S. R. Foltyn, A. T. Findikoglu, P. Tiwari, J. P. Zheng, and T. R. Jow, "Heteroepitaxial growth of highly conductive metal oxide RuO₂ thin films by pulsed laser deposition," *Applied Physics Letters* **67**, 1677 (1995).
- ⁹⁷M. J. Abb, T. Weber, L. Glatthaar, and H. Over, "Growth of Ultrathin Single-Crystalline IrO₂(110) Films on a TiO₂(110) Single Crystal," *Langmuir* **35**, 7720–7726 (2019).
- ⁹⁸W. Braun and J. Mannhart, "Film deposition by thermal laser evaporation," *AIP Advances* **9**, 085310 (2019).
- ⁹⁹J. P. Zheng and H. S. Kwok, "Low resistivity indium tin oxide films by pulsed laser deposition," *Applied Physics Letters* **63**, 1–3 (1993).
- ¹⁰⁰P. Adiga, W. Nunn, C. Wong, A. K. Manjeshwar, S. Nair, B. Jalan, and K. A. Stoerzinger, "Breaking OER and CER scaling relations via strain and its relaxation in RuO₂ (101)," *Materials Today Energy* **28**, 101087 (2022).
- ¹⁰¹A. M. Serventi, M. A. E. Khakani, R. G. Saint-Jacques, and D. G. Rickerby, "Highly textured nanostructure of pulsed laser deposited IrO₂ thin films as investigated by transmission electron microscopy," *Journal of Materials Research* **16**, 2336–2342 (2001).
- ¹⁰²Y. Wang, S. Lee, P. Vilmercati, H. N. Lee, H. H. Weitering, and P. C. Snijders, "Atomically flat reconstructed rutile TiO₂(001) surfaces for oxide film growth," *Applied Physics Letters* **108**, 8–10 (2016).
- ¹⁰³W. S. Choi, S. S. A. Seo, K. W. Kim, T. W. Noh, M. Y. Kim, and S. Shin, "Dielectric constants of Ir, Ru, Pt, and IrO₂ : Contributions from bound charges," *Physical Review B* **74**, 205117 (2006).
- ¹⁰⁴A. K. Goel, G. Skorinko, and F. H. Pollak, "Optical properties of single-crystal rutile RuO₂ and IrO₂ in the range 0.5 to 9.5 eV," *Physical Review B* **24**, 7342–7350 (1981).
- ¹⁰⁵In case this procedure does not produce a closed film at the reported laser energy density, we suggest to initially vary this parameter by several 100 mJ/cm², as optical parameters can vary strongly between PLD setups.
- ¹⁰⁶H.-D. Kim, H.-J. Noh, K. H. Kim, and S.-J. Oh, "Core-Level X-Ray Photoemission Satellites in Ruthenates: A New Mechanism Revealing The Mott Transition," *Physical Review Letters* **93**, 126404 (2004).
- ¹⁰⁷M. L. Green, M. E. Gross, L. E. Papa, K. J. Schnoes, and D. Brasen, "Chemical Vapor Deposition of Ruthenium and Ruthenium Dioxide Films," *Journal of the Electrochemical Society* **132**, 2677–2685 (1985).
- ¹⁰⁸A. Dahal, H. Coy-Diaz, R. Addou, J. Lallo, E. Sutter, and M. Batzill, "Preparation and characterization of Ni(111)/graphene/Y₂O₃(111) heterostructures," *Journal of Applied Physics* **113** (2013), 10.1063/1.4805042.
- ¹⁰⁹F. Krizek, Z. Kašpar, A. Vetushka, D. Krieger, E. M. Fiordaliso, J. Michalicka, O. Man, J. Zubáč, M. Brajer, V. A. Hills, K. W. Edmonds, P. Wadley, R. P. Campion, K. Olejník, T. Jungwirth, and V. Novák, "Molecular beam epitaxy of CuMnAs," *Physical Review Materials* **4** (2020), 10.1103/PhysRevMaterials.4.014409, 1911.01794.
- ¹¹⁰X. Yang, P. Gao, Z. Yang, J. Zhu, F. Huang, and J. Ye, "Optimizing ultrathin Ag films for high performance oxide-metal-oxide flexible transparent electrodes through surface energy modulation and template-stripping procedures," *Scientific Reports* **7**, 1–9 (2017).
- ¹¹¹M. Petit, R. Hayakawa, Y. Wakayama, and T. Chikyw, "Early stage of growth of a perylene diimide derivative thin film growth on various Si(001) substrates," *Journal of Physical Chemistry C* **111**, 12747–12751 (2007).
- ¹¹²R. Martin, M. Kim, C. J. Lee, V. Mehar, S. Albertin, U. Hejral, L. R. Merte, E. Lundgren, A. Asthagiri, and J. F. Weaver, "High-Resolution X-ray Photoelectron Spectroscopy of an IrO₂(110) Film on Ir(100)," *The Journal of Physical Chemistry Letters* **11**, 7184–7189 (2020).
- ¹¹³S. J. Freakley, J. Ruiz-Esquivius, and D. J. Morgan, "The X-ray photoelectron spectra of Ir, IrO₂ and IrCl₃ revisited," *Surface and Interface Analysis* **49**, 794–799 (2017).
- ¹¹⁴N. Fairley, V. Fernandez, M. Richard-Plouet, C. Guillot-Deudon, J. Walton, E. Smith, D. Flahaut, M. Greiner, M. Biesinger, S. Tougaard, D. Morgan, and J. Baltrusaitis, "Systematic and collaborative approach to problem solving using X-ray photoelectron spectroscopy," *Applied Surface Science Advances* **5**, 100112 (2021).
- ¹¹⁵C. Ma and C. Chen, "Pulsed Laser Deposition for Complex Oxide Thin Film and Nanostructure," in *Advanced Nano Deposition Methods* (Wiley, 2016) pp. 1–31.
- ¹¹⁶N. A. Shepelin, Z. P. Tehrani, N. Ohannessian, C. W. Schneider, D. Pergolesi, and T. Lippert, "A practical guide to pulsed laser deposition," *Chemical Society Reviews* **52**, 2294–2321 (2023).
- ¹¹⁷Y. Liu, H. Masumoto, and T. Goto, "Preparation of IrO₂ Thin Films by Oxidating Laser-ablated Ir," *MATERIALS TRANSACTIONS* **45**, 900–903 (2004).
- ¹¹⁸M. J. S. Abb, T. Weber, D. Langsdorf, V. Koller, S. M. Gericke, S. Pfaff, M. Busch, J. Zetterberg, A. Preobrajenski, H. Grönbeck, E. Lundgren, and H. Over, "Thermal Stability of Single-Crystalline IrO₂ (110) Layers: Spectroscopic and Adsorption Studies," *The Journal of Physical Chemistry C* **124**, 15324–15336 (2020).
- ¹¹⁹E. H. P. Cordfunke and G. Meyer, "The system iridium - oxygen I. Measurements on the volatile oxide of iridium," *Recueil des Travaux Chimiques des Pays-Bas* **81**, 495–504 (1962).
- ¹²⁰B. R. Chalamala, Y. Wei, R. H. Reuss, S. Aggarwal, B. E. Gnade, R. Ramesh, J. M. Bernhard, E. D. Sosa, and D. E. Golden, "Effect of growth conditions on surface morphology and photoelectric work function characteristics of iridium oxide thin films," *Applied Physics Letters* **74**, 1394–1396 (1999).
- ¹²¹Y. Liu, H. Masumoto, and T. Goto, "Electrical and Optical Properties of IrO₂ Thin Films Prepared by Laser-ablation," *MATERIALS TRANSACTIONS* **45**, 3023–3027 (2004).